The dissolved oxygen ramp is immoral: facing global water challenges with mathematical analysis

Mariane Y. Schneider*,
BIOMATH, Department of Data Analysis and Mathematical Modelling,
Ghent University, Coupure Links 653, Ghent 9000, Belgium
DTU Sustain, DTU, Anker Engelunds Vej 101,
Building 101, 2800 Kongens Lyngby, Denmark
*corresponding author: `mariane.schneider@ugent.be`

Elena Torfs
modelEAU, Département de génie civil et de génie des eaux, Université Laval,
pavillon Adrien-Pouliot, 1065, av. de la Médecine, Québec, G1V 0A6, Canada
`elena.torfs@gci.ulaval.ca`

Juan Pablo Carbajal
Institute for Energy Technology, OST Eastern Switzerland University of Applied Sciences,
Oberseestrasse 10, 8640 Rapperswil, Switzerland
`juanpablo.carbajal@ost.ch`

February 2025

Abstract

The water sector is increasingly relying on data-driven approaches to create proxy measurements. These approaches are often trained with data covering only few situations, resulting in a lack of robustness and increasing the risk of false predictions. Therefore, robust approaches are needed for data-driven proxy measurements (i.e. soft sensors), especially for water recovery and reuse. In climate science and robotics, Dynamical Systems Analysis (DSA) is used to explore a wide range of system behaviour and uncover conditions of high uncertainty, and potential tipping points. DSA allows the systematic analysis of model dynamics, and the measurable features caused by these dynamics. We created a novel DSA workflow for soft-sensor development to measure water quality. Herein, we demonstrate that the integration of DSA into soft-sensor development adds robustness by revealing all mathematically possible combinations of state variables that lead to a feature. It can thus detect possible interferences and help design the soft sensor to avoid these. We used DSA for the falsification of a ramp-feature-based soft sensor and found that, despite a published, successful laboratory and real-world application, the ramp feature is immoral. Such an immorality implies that false predictions could occur. However, the DSA analysis uncovered under which operational conditions the ramp becomes a robust soft sensor feature. Targeted experiments will be necessary to confirm the boundary of the robust conditions in the real world.

Contents

1 Introduction **2**

2 Results and Discussion **5**
2.1 Model dependency graph . . . 5
2.2 The dissolved oxygen ramp feature in detail . . . 5
2.3 Identification of states leading to dissolved oxygen ramps . . . 6
2.4 Immorality of the dissolved oxygen ramp . . . 8
2.5 Ramp points distribution . . . 8
2.6 Limitations and outlook . . . 9

3 Conclusion **10**

4 Materials and methods **10**
4.1 Dissolved oxygen feature 10
4.2 Model signal features 11
4.3 Model structure 11
4.4 Ramp contingency 12

A Supplementary information **17**
A.1 Time derivatives 17
A.1.1 Single state actuation 18

B Ramp points curve **18**
B.1 Interpretability of the inflection point curve 20
B.2 Symbols name 20
B.3 ASM1 model 20

C Causal diagram **25**
C.1 Ammonium depletion soft-sensor based on the dissolved oxygen ramp feature 26

Glossary

ADM Anaerobic Digestion Model. 3, 4, 10, 12

ASM Activated Sludge Model. 3–6, 8–12, 18, 25

BSM Benchmark Simulation Model. 4, 25

DSA Dynamical Systems Analysis. 1, 3–11, 26

ODE Ordinary Differential Equation. 3

ramp A time-based signal feature. It is defined as the signal's non-saddle (non-zero first time derivative) inflection point (zero second time derivative).. 2, 5–12, 18–21, 25, 26

SBR Sequencing Batch Reactor. 5, 10

1 Introduction

The impact of climate change on water cycles has a cascading effect on urban areas, agriculture, industry, and the natural environment, necessitating adaptation. A flexible, circular on-site infrastructure [1–3], is a promising adaptation strategy. Furthermore, on-site plants may allow cost savings by removing the need for sewer infrastructure [4].

Monitoring and control pose decisive challenges inherent to on-site water and wastewater infrastructure. This can be attributed, on the one hand, to the high capital cost required to purchase physical water quality sensors. One way to reduce these costs is developing soft sensors [5] based on inexpensive proxy sensors instead. On the other hand, monitoring is hampered by required sensor maintenance [6]. Most studies do not address the maintenance challenge even for on-site settings [e.g. 7, 8]. However, sensors expose a variety of often non-linear wearing effects such as damage, fouling, or deterioration [e.g. 9–12] and sensor faults that impact the treatment performance [13]. The wearing effects are especially challenging for data-driven approaches, despite accurate results [e.g. 14]. The reason is that wearing effects cause measurements that can lie outside the training dataset. Consequently, sensors should either be installed in an environment where nearly no maintenance is required, for example, a chlorination tank [15] or features for monitoring [16] and control [17] need to be robust to sensor wearing effects such as drift or noise by design.

Schneider et al. [16] directly compared a soft sensor to predict complete ammonia oxidation using a ramp feature (i.e. a non-saddle inflection point, see "Ramp" in fig. 7) in the dissolved oxygen signal based on data from maintained and unmaintained sensors. The ammonium-depletion detection based on the ramp feature are robust by design to most effects from noise, measurement uncertainties, or effects of sensor wearing by relying on the qualitative trend instead of absolute values and including a low-pass filter. Nevertheless, three time-consuming sampling campaigns revealed at least two alternative causes for the dissolved-oxygen ramp feature i.e. the aeration pattern and alkalinity limitation. Additionally, in silico experiments based on synthetic data generated with SUMO [18] revealed that short solids retention time [6] can cause a false predictions (see fig. 1. Hence, designing robust soft sensors is constrained by our ability to systematically explore the causes of the feature, e.g. due to the plethora of state combinations that can lead to it. Moreover, the presence of alternative causes for the feature (see the supplementary information sec. C) poses a risk of erroneous soft-sensor predictions, potentially affecting human and

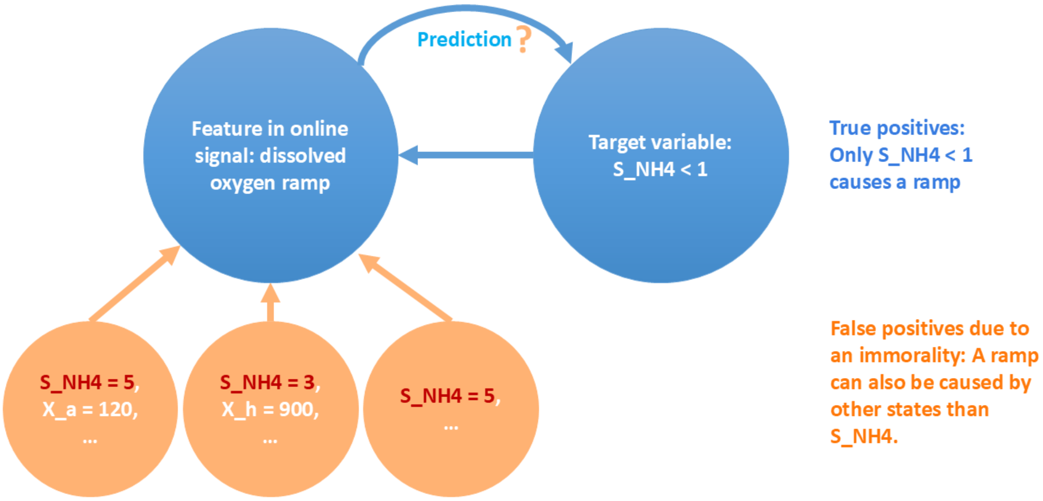

Figure 1: Schematic explanation of immorality, true and false positive predictions. S_{NH4} represents the target variable in this case, the ammonium concentration. X_{a} (the autotrophic bacteria) and X_{h} (the heterotrophic bacteria) are states involved in an immorality and could lead to false predictions. This can occur with any other state variable, excluding the target variable, that is used to predict the feature.

environmental health. To avoid these undesired effects, a systematic identification of the alternative causes and the analysis of the plausibility of their occurrence is required.

For complex systems such as the human brain, global weather, or biochemical wastewater treatment processes, understanding the functional architecture is crucial for defining effective, rigorous, principled, and general methods, yet remains a challenge [19]. To find such a method, we systematically analyse sets of Ordinary Differential Equations (ODE) using an approach that we call Dynamical Systems Analysis (DSA) [see 20, for a joyful introduction]. The approach aims at understanding a set of ODEs without integrating them, usually leading to efficient workflows and adding a novel perspective to problem-solving. DSA encompasses techniques for characterising stability and bifurcations (cf. tipping points), and allows screening any dynamic model for a plethora of features. In other fields, such as robotics, DSA is frequently employed [21–23, e.g.] to gain mathematical insights into the engineering problem at hand, which more often than not leads to novel solutions. In climate science, DSA has been used to predict abrupt changes like tipping points [24]. DSA also provides an alternative perspective into model calibration [25, ch. 1], which focuses on validating structural features of the model with experimental data, as opposed to the more conventional approach of matching time series. Due to all these properties, we hypothesise that an improved understanding of model dynamics with DSA is crucial for engineering features for robust monitoring and control.

In wastewater treatment, DSA remains an uncommon approach. When DSA is employed, it is frequently referred to with ambiguous terms like "analysis", which hinders identifying relevant studies. We, therefore, believe that a review on DSA applied in biochemical treatment and recovery processes of wastewater and similar streams is timely, especially to the popular Activated Sludge Model (ASM) [26] and Anaerobic Digestion Model (ADM) [27]. Hence, we provide a brief one in tab. 1.

Reference	**Model**	**DSA outcome**	**Implication/application**
Vanrolleghem [28]	ASM1 and solid flux sedimentation model	Implication of degradation and settling for control design	Improved control design
Grognard and Bernard [29]	Two-population model for anaerobic processes	Stability analysis with non-trivial solutions	Avoiding instability e.g. acidification
Shen et al. [30]	Anaerobic digestion	Identified three stable points, and a saddle-node bifurcation under typical operation conditions	Identification of stable operating conditions
Nelson and Sidhu [31]	ASM1	Identified two branch points	Determination of optimalresidence time
Volcke et al. [32]	Two-step biological conversion system	Identification of steady state multiplicity	Experimental design
Benyahia et al. [33]	Two-step ADM	Bifurcation and stability analysis	Experimental design for a soluble microbial products monitoring strategy
Bornhöft et al. [34]	ADM1	Bifurcation analysis	Model selection: Impact of model simplification
Dionisi et al. [35]	Two-population model in a batch process	Stability analysis	Accelerate calculations to reach steady state
Wade and Wolkowicz [36]	Impulsive annamox	Bifurcation analysis	Prediction of wash-out of nitrite-oxidising bacteria
Neto et al. [37]	Benchmark Simulation Model1 (BSM)	Structural controllability and observability	Stability, controllability and observability
Sampaio et al. [38]	ASM1 extended for greenhouse-gas emissions, two-step nitrification, four-step denitrification, and 10-layer settling	Structural analysis	Full-state controllability and observability of greenhouse gas emissions

Table 1: Literature review on DSA in anaerobic digestion and activated sludge modelling for wastewater treatment.

These successful examples from the water sector indicate the value of DSA for analysing steady states and stability. These analyses contribute to the identification of regions of optimal operation, control, or observability, and experimental design. However, the use in other fields shows, that the potential of DSA is far from exhausted in the water sector. We deduce that systematic detection of information-rich system dynamics (i.e. features) merits further attention, with applications in feature-based model calibration and feature engineering for soft-sensor development, the latter being the primary focus of this study.

2 Results and Discussion

Herein, we showcase DSA for qualitative trend feature-based soft-sensor development. To model the activated sludge process we used the mass balance-corrected version of ASM1 [39] by Hauduc et al. [40]. We exemplify the use of DSA for feature engineering by systematically investigating factors affecting the ramp feature in the dissolved oxygen signal in a Sequencing Batch Reactor (SBR) to predict the effluent ammonium concentration. The current work complements previous data-driven, mechanistic, or hybrid feature-learning approaches [41] on a process familiar to the authors to introduce and discuss DSA as a potential standard procedure for soft-sensor development.

2.1 Model dependency graph

A worthwhile first step to get an overview before performing a DSA is a visual inspection of the dependencies. The dependency graph implies causation from the relations between states defined in the analysed model. Figure 2 shows the dependency graph of the 14 states of the mass balance-corrected ASM1 Hauduc et al. [40]. The many circular dependencies reflect the high complexity of the system. Furthermore, all processes follow the pattern state→rate→state, which hints at the specific model structure presented in sec. 2.3. By looking at the arrows and their direction, we can identify that five of these states do not affect the dynamics of the other states, of which two are uncoupled (no children or parents in the graph, i.e. $X_{\mathrm{nb,in}}$, S_{nb}), and three are measurements (no children, i.e. $X_{\mathrm{nb,e}}$, S_{N2}, S_{alk}). Therefore, the dynamics of ASM1 are determined by the following nine states (in brackets is the notation by Henze et al. [39]):

S_{b}	Soluble biodegradable organics (SS)
X_{cb}	Particulate and colloidal biodegradable organics (XS)
X_{h}	Ordinary heterotrophic organisms (XBH)
X_{a}	Autotrophic nitrifying organisms (NH4+ to NO3-, XBA)
S_{O2}	Dissolved oxygen (SO)
S_{NOx}	Nitrate and nitrite (NO3 + NO2) (considered to be NO3 only for stoichiometry, SNO)
S_{NHx}	Ammonia (NH4 + NH3) (SNH)
S_{bN}	Soluble biodegradable organic N (SND)
X_{cbN}	Particulate and colloidal biodegradable organic N (XND)

2.2 The dissolved oxygen ramp feature in detail

To illustrate the traditional way of finding inflection points (i.e. ramp features), we show in fig. 3 the time-series of the states of ASM1 generated by one set of initial conditions. With S_{O2} and S_{NHx} in the top panel true and false positive (see fig. 1 for a definition) ramp features can be identified in this single batch run. The vertical lines represent time instances where the conditions of a ramp in the oxygen signal (defined in equations (9)-(10)) are satisfied.

The first ramp in the S_{O2} signal is particularly interesting. If the soft sensor does not identify this ramp correctly to stop the treatment process, the ammonium concentration starts rising. The relevant process is the ammonification during the decay of heterotrophic bacteria in the absence of sufficient autotrophic bacteria. The second ramp is a false positive one. The third ramp is what we generally would expect in a biochemical treatment process that recovers wastewater batch-wise. Remarkable is also that the two true positive ramps have a much steeper slope than the false positive one. The first objective of the present work is to use DSA to efficiently screen for potential causes of false positives in the ramp feature, in other words to identify when the soft sensor fails to estimate the ammonium concentration correctly. Another objective is to explore the potential of DSA to make the ramp feature more robust.

Formally, ramps are zeros of the second time derivative in which the first derivative is positive (i.e. non-saddle inflection point). The locus, i.e. the set of all points that satisfy the specified conditions, of ramps can be described mathematically by:

$$\text{ramps} \coloneqq \{t : \dot{x}(t) > 0 \land \ddot{x} = 0\} \tag{1}$$

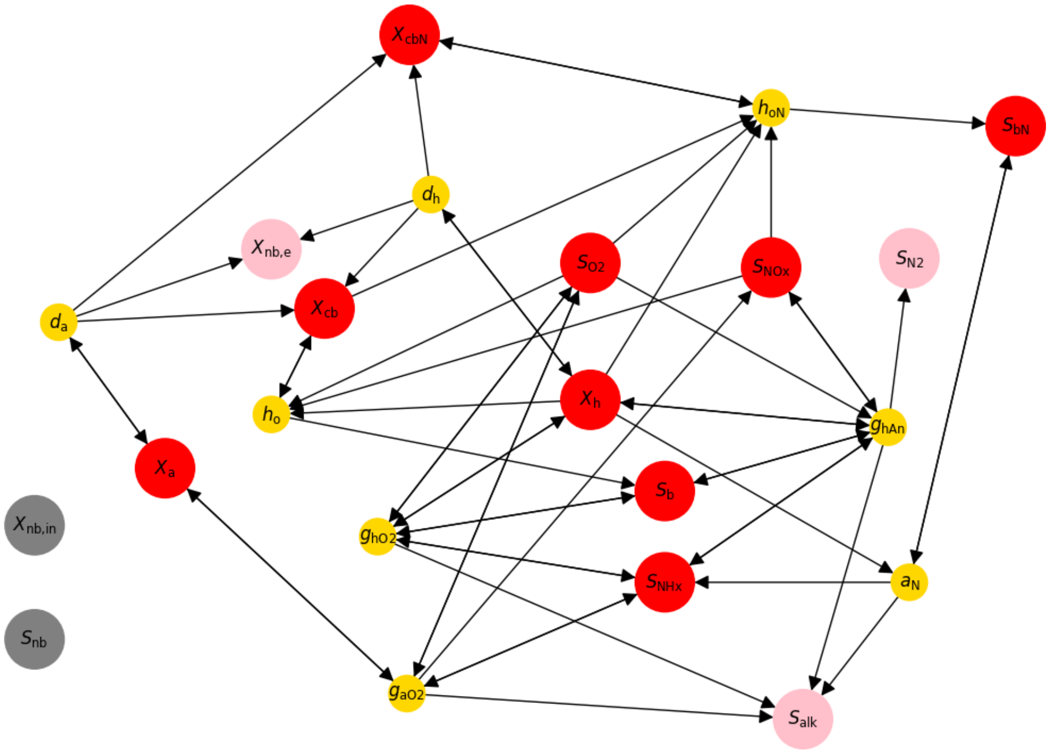

Figure 2: ASM1 state dependency graph. The graph depicts the interactions between the states in the model. States (larger nodes) affect rates (smaller nodes), which in turn affect the states through their time derivative. The arrows indicate which states and rates affect each other. Pink nodes with no child are measurements which do not impact other states. Grey nodes with neither parent nor child are uncoupled (i.e. the non-biodegradable organics, S_{nb}, and particulate non-biodegradable organics from the influent, $X_{\mathrm{nb,in}}$). The red nodes are the potential alternative causes for the ramp feature that would lead to a false prediction of the target variable.

where the signal is given by $x(t)$, the doted symbols represent time derivatives, and the wedge ($\wedge$) is the logical conjunction (and) symbol, meaning that both criteria need to be fulfilled simultaneously.

2.3 Identification of states leading to dissolved oxygen ramps

To identify the states that lead to a ramp feature in the dissolved oxygen signal (represented by the state S_{O2}), we need to compute the second time derivative of this state (i.e. $\ddot{S}_{\mathrm{O2}}$), see equation (13). This derivative can be computed directly from the model equations without having to simulate the full set of equations to generate a signal, making DSA a compelling and computationally efficient method. This computation can be done for any model structure, but for the ASM family the computations are simplified thanks to the structure of the model that can for example be identified from fig. 2:

$$\dot{\boldsymbol{x}} = \mathtt{M}\,\boldsymbol{r}(\boldsymbol{x}) + \boldsymbol{z} \tag{2}$$

$$\ddot{\boldsymbol{x}} = \mathtt{M}\,\dot{\boldsymbol{r}} + \dot{\boldsymbol{z}} = \mathtt{M}\,\mathtt{J}_{\boldsymbol{r}}\,\dot{\boldsymbol{x}} + \dot{\boldsymbol{z}} \tag{3}$$

where we used boldface, e.g. $\boldsymbol{x}$, for vectors, and capital typewriter font, e.g. $\mathtt{M}$ for matrices. In equation (2), $\boldsymbol{x}$ is the vector of states of the model. The states are then transformed via the mapping $\boldsymbol{r}(\boldsymbol{x})$, into a new vector, which herein we will call *rates* vector. The matrix $\mathtt{M}$, such as the stoichiometric matrix Gujer and Henze [42], combines the rates to produce the time derivatives of the states. The additional term ($\boldsymbol{z}$) in equation (2) represents the *actuation* on the states of the system. More details and explanations are given in sec. 4.3. Therefore, if the autonomous parts of the model, $\mathtt{M}$ and $\boldsymbol{r}(\boldsymbol{x})$, are given in tabular form, we can evaluate equations (2) and (3) directly, which allows to analyse any features based on the time derivatives of the model states.

Applying these formulae to ASM1 (given in supplementary information B.3), we obtain equations for the first and second time derivative of the dissolved-oxygen state (S_{O2}). For the first derivative, we get:

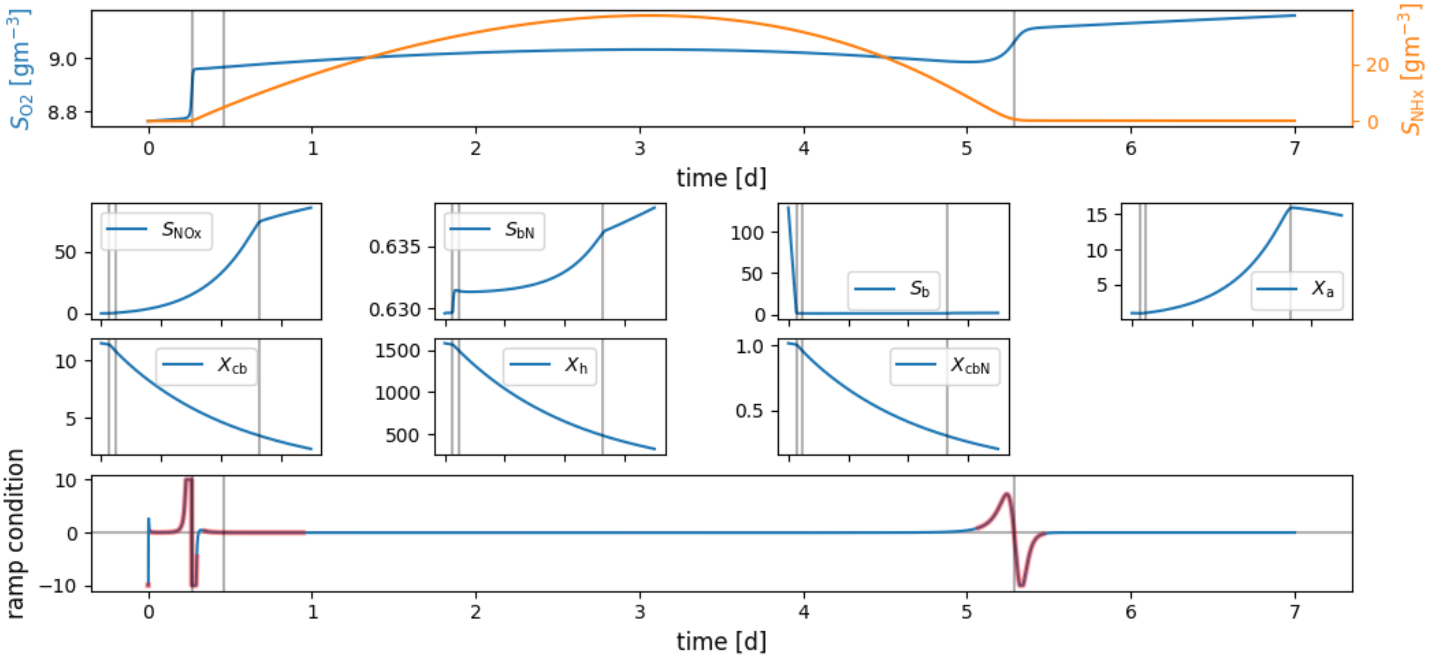

Figure 3: The top panel shows the dissolved oxygen (S_{O2}) and the effluent ammonium (S_{NHx}) concentration signals. The ramp time instances are marked on all panels as vertical lines and the time intervals on the x-axes are the same. The second ramp (close to 0.5 d) is a false positive for the effluent ammonium concentration estimation, the third one (close to 5.25 d) is a true positive feature, and the first one (close to 0.25 d) is a true positive that is not caused by the ammonium reaching a concentration below the threshold at the ramp-occurrence time, but the ammonium is already low before the ramp. Possible causes for the ramp feature can be identified by looking at the other panels, showing other state variables of the model (see list in page 5). Each of these three ramp observations corresponds with one point on an inflection point curve. The time series are generated for one single set of initial conditions, and are shown here to display the ramp feature detection. These time series would not be simulated when DSA is used to obtain the inflection point curves. The units of all state variables are g m^{-3}.

$$\dot{S}_{\mathrm{O2}} = m_{S_{\mathrm{O2}}\,g_{\mathrm{aO2}}}\, g_{\mathrm{aO2}}(S_{\mathrm{NHx}}, S_{\mathrm{O2}}, X_{\mathrm{a}}) + m_{S_{\mathrm{O2}}\,g_{\mathrm{hO2}}}\, g_{\mathrm{hO2}}(S_{\mathrm{NHx}}, S_{\mathrm{O2}}, S_{\mathrm{b}}, X_{\mathrm{h}}) + z_{\mathrm{O2}} \tag{4}$$

$$m_{S_{\mathrm{O2}}\,g_{\mathrm{aO2}}} := \frac{\gamma_{\mathrm{a}} + \iota_{\mathrm{COD,NO3}}}{\gamma_{\mathrm{a}}} \qquad m_{S_{\mathrm{O2}}\,g_{\mathrm{hO2}}} := \frac{\gamma_{\mathrm{h}} - 1}{\gamma_{\mathrm{h}}} \tag{5}$$

$$g_{\mathrm{aO2}}(S_{\mathrm{NHx}}, S_{\mathrm{O2}}, X_{\mathrm{a}}) := \mu_{\mathrm{max,a}}\, X_{\mathrm{a}} \frac{S_{\mathrm{NHx}} S_{\mathrm{O2}}}{(S_{\mathrm{NHx}} + \kappa_{\mathrm{NHx,a}})\,(S_{\mathrm{O2}} + \kappa_{\mathrm{O2,a}})} \tag{6}$$

$$g_{\mathrm{hO2}}(S_{\mathrm{NHx}}, S_{\mathrm{O2}}, S_{\mathrm{b}}, X_{\mathrm{h}}) := \mu_{\mathrm{max,h}}\, X_{\mathrm{h}} \frac{S_{\mathrm{NHx}} S_{\mathrm{O2}} S_{\mathrm{b}}}{(S_{\mathrm{NHx}} + \kappa_{\mathrm{NHx,h}})\,(S_{\mathrm{O2}} + \kappa_{\mathrm{O2,h}})\,(S_{\mathrm{b}} + \kappa_{\mathrm{b}})} \tag{7}$$

Since the biological activity of heterotrophic and autotrophic bacteria consumes dissolved oxygen, the first two terms are always non-positive. The signs of $m_{S_{\mathrm{O2}}\,g_{\mathrm{aO2}}}$ and $m_{S_{\mathrm{O2}}\,g_{\mathrm{hO2}}}$ are determined by the coefficients in equation (5), and for plausible values of γ_a and γ_h (see tab. 4), these signs are negative.

In the equations above we explicitly show the dependency of the rates (states in parentheses) that we extracted from the model equations. We omit them in the formulae for the second derivative:

$$\begin{aligned}
\ddot{S}_{\mathrm{O2}} =& \dot{S}_{\mathrm{NHx}}\, \partial_{S_{\mathrm{NHx}}} \left(g_{\mathrm{aO2}}\, m_{S_{\mathrm{O2}}\,g_{\mathrm{aO2}}} + g_{\mathrm{hO2}}\, m_{S_{\mathrm{O2}}\,g_{\mathrm{hO2}}}\right) \\
&+ \dot{S}_{\mathrm{O2}}\, \partial_{S_{\mathrm{O2}}} \left(g_{\mathrm{aO2}}\, m_{S_{\mathrm{O2}}\,g_{\mathrm{aO2}}} + g_{\mathrm{hO2}}\, m_{S_{\mathrm{O2}}\,g_{\mathrm{hO2}}}\right) \\
&+ \dot{S}_{\mathrm{b}} \partial_{S_{\mathrm{b}}} g_{\mathrm{hO2}}\, m_{S_{\mathrm{O2}}\,g_{\mathrm{hO2}}} + \dot{X}_{\mathrm{a}} \partial_{X_{\mathrm{a}}} g_{\mathrm{aO2}}\, m_{S_{\mathrm{O2}}\,g_{\mathrm{aO2}}} + \dot{X}_{\mathrm{h}} \partial_{X_{\mathrm{h}}} g_{\mathrm{hO2}}\, m_{S_{\mathrm{O2}}\,g_{\mathrm{hO2}}} \\
&+ z_{\mathrm{O2}}\, \partial_{S_{\mathrm{O2}}} \left(g_{\mathrm{aO2}}\, m_{S_{\mathrm{O2}}\,g_{\mathrm{aO2}}} + g_{\mathrm{hO2}}\, m_{S_{\mathrm{O2}}\,g_{\mathrm{hO2}}}\right) + \dot{z}_{\mathrm{O2}}
\end{aligned} \tag{8}$$

The conditions for the ramp (section 4.2) read:

$$\dot{S}_{\mathrm{O2}} > 0 \tag{9}$$

$$\ddot{S}_{\mathrm{O2}} = 0 \tag{10}$$

The first condition for a ramp, equation (9), requires a positive time derivative. This expresses that the rate at which oxygen is transferred to the liquid phase (z_{O2}) needs to be bigger than the oxygen uptake rate by the bacteria, as there

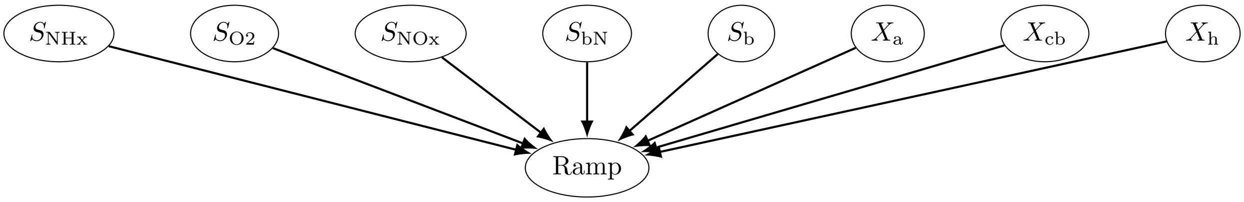

Figure 4: Causes of the dissolved oxygen (S_{O2}) ramp feature. Obtained from the variables in equation (8). Several V-structures are identified from the causal relations. See list in page 5 for the variable names.

cannot be more oxygen consumed than is present. Therefore, in ASM1 the dissolved oxygen ramp is a feature that can only be generated with a source of dissolved oxygen (aeration) as otherwise equation (9) cannot be fulfilled. This underlines the role of aeration for the detection and robustness of the ramp feature, which in a different context, was observed in a real-world case in [6].

Using DSA shows that the conditions (9) and (10) depend on other states besides S_{NHx} and S_{O2}, i.e. $S_{\mathrm{NOx}}, S_{\mathrm{bN}}, S_{\mathrm{b}}, X_{\mathrm{a}}, X_{\mathrm{cb}}, X_{\mathrm{h}}$. So, even if we kept S_{NHx} constant at a value above the prediction threshold for a full ammonium depletion, changes to these other states could generate a ramp that is not due to a S_{NHx} below this threshold. This can potentially lead to false positive predictions with a ramp-based soft sensor.

2.4 Immorality of the dissolved oxygen ramp

From the nine states in the dependency graph (fig. 2), DSA shows that eight states are actual causes of a ramp, X_{cbN} is not a cause. These eight states form several V-structures within the causal diagram of the ramp feature in fig. 4; known as *immoralities* [43]. The states (parents) in a V-structure, will be associated (correlated) when data is selected conditional on the presence of the feature (child). These correlations can be exploited by a data-driven machine learning model to infer difficult-to-monitor states, e.g. S_{NHx} from S_{O2}, or to alleviate an effluent ammonium prediction task. However, since pure data-driven approaches are limited to exploiting correlations without guaranteeing causality; adding causal relations, as we do here, can enhance the performance and information extracted from the method, e.g. to include root cause analysis and therewith improve the robustness of the sensor.

DSA allows the systematic evaluation of conditions that lead to a ramp in a search process by sampling the states independently to determine the causes (parents) of the ramp feature, see fig. 4. This is illustrated in fig. 5a which shows all ramps found on the (S_{O2}, S_{NHx}) plane for 10,000 uniformly distributed random values of all the other six states that can cause ramps (see section B for explanations on how to read these curves). Each line is a 0-level set curve of equation (10) that satisfies equation (9). Figure 5a further shows that many of these ramps are below an arbitrary threshold of $1\,\mathrm{g\,m^{-3}}$ $S_{\mathrm{NHx\text{-}N}}$. All the ramps below the threshold would lead to the correct conclusion that the ammonium oxidation process is complete (true positive), hence the feature is informative. However, many other ramps are clearly above the threshold, and would lead to an erroneous conclusion (false positive).

To further investigate these false positives, fig. 5b shows all ramps found on the (S_{O2}, X_{a}) plane for the autotrophic bacteria. We chose the autotrophic bacteria because they are responsible for the removal of nitrogen compounds such as ammonium. Therefore, we have only sampled values of S_{NHx} above the arbitrary threshold, between $1\,\mathrm{g\,m^{-3}}$ to $200\,\mathrm{g\,m^{-3}}$. For all other states, we used the same ranges as before. Hence, only false positive ramps are shown in this plot. This allows us to evaluate the causes of false positive results and identify measures to increase accuracy. The pattern clearly shows that a high concentration of X_{a} could drastically reduce the false positive results.

In summary, fig. 5a and fig. 5b illustrate how DSA can be used to systematically scan a feature space for the occurrence of features and their causes. Analysing the equations allows us to identify causal relations, which is very different from checking data for correlation. For an extended discussion of these results concerning experimental work in [6, 16] see sec. C.1.

2.5 Ramp points distribution

Figure 6 shows the distribution of states that cause a ramp feature (satisfy equations (9)- (10)). Blue and orange dots indicate effluent ammonium concentrations below and above an arbitrary threshold (T), respectively. Blue dots are thus true positives for the ammonium soft sensor and orange dots represent false positives (compare fig. 1). The plot also shows the dissolved oxygen time derivative ($\dot{S}_{\mathrm{O2}}$) at these points. We observed in fig. 3 that true ramps are associated with higher derivatives than false ramps. The top right panel of fig. 6 (S_{NHx} vs $\dot{S}_{\mathrm{O2}}$) supports this observation, as almost no false ramps are found above dissolved oxygen time derivatives of $400\,\mathrm{g\,m^{-3}\,d^{-1}}$ Therefore, using time derivative information (slope in a time series plot) together with the detection of ramps constitutes a more accurate feature.

This observation also provides a plausible explanation for the improved accuracy of an ammonium depletion classifier when slope information was included. Without a restriction on the slope the feature was not informative [6, 16]. In these previous studies this slope restriction was found with trial and error, while DSA offers a systematic approach. ASM1 already captures this relation, despite missing processes and its relative simplicity compared to other activated sludge models. Identifying such

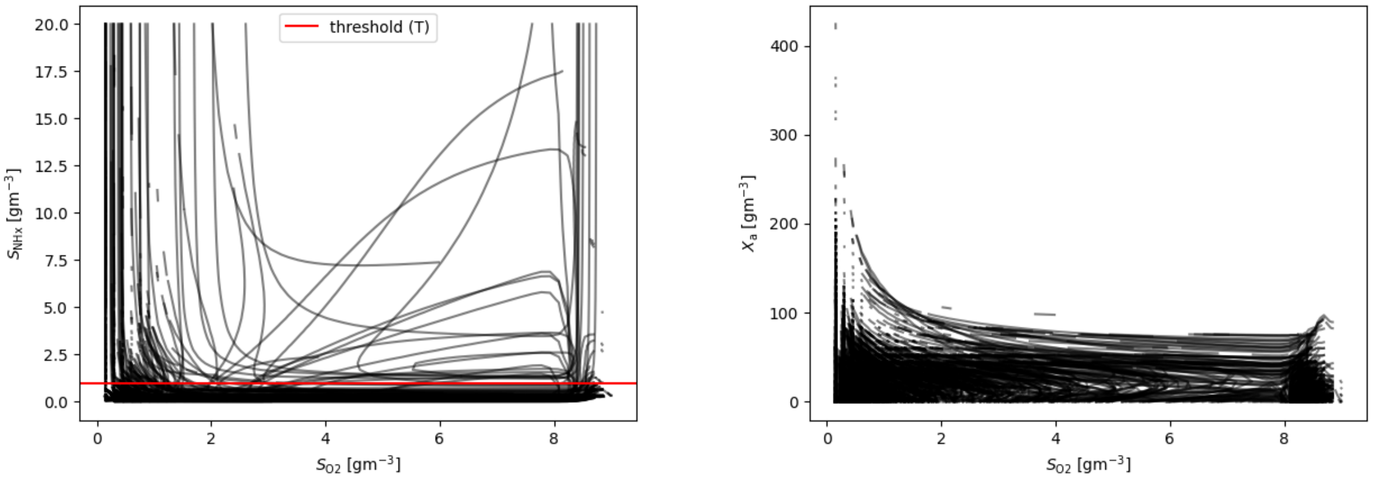

(a) Locus of all ramps in the (S_{O2}, S_{NHx}) plane.

(b) Locus of false positive ramps in the (S_{O2}, X_{a}) plane

Figure 5: Inflection point curves in two planes. The lines show the combinations of S_{O2} and S_{NHx} or S_{O2} and X_{a} that lead to a ramp feature. 10,000 simulations with different initial conditions for each panel were conducted. The darker the area, the more overlapping inflection points are in the region. The ammonium concentrations for b) were restricted to only show panels with false positive ramps i.e. the ammonium concentration is above an arbitrary threshold of $1\,\mathrm{g\,m^{-3}}$.

a slope dependence shows that for the ramp-feature design ASM1 is structurally useful. Therefore, we demonstrate that and how DSA can be used for structural model verification.

In the top right panel of fig. 6 we further observe that eliminating the false positives by defining a minimal slope and rejecting all ramps below the chosen slope (e.g. $< 400\,\mathrm{g\,m^{-3}\,d^{-1}}$) may result in many false negatives. The coloured shaded regions for different levels of X_{a} indicate that with a higher X_{a} the slope tolerance could be considerably lowered to reduce the false negatives. Hence, finding another feature or sensor to estimate X_{a} would increase the accuracy of the ramp-based soft sensor.

Further patterns can be recognised in fig. 6- For example if S_{bN} is above approximately $7\,\mathrm{g\,m^{-3}}$, no correct predictions may be possible. It is reasonable to think that if the soluble biodegradable organic nitrogen is high, too much ammonium is formed, and its concentration drop is limited. The experimental confirmation of this discovery is part of future work. Furthermore, observing multiple additional patterns in fig. 6 to the ones discussed in this article shows great potential for future studies, e.g., to further improve the soft sensor with an estimate X_{a} or to identify an early warning feature for loss of nitrifying biomass. Additionally, the results of the DSA hint at which regions could be used by data-driven models.

Herein, we demonstrated how DSA can be used to improve the feature, e.g. by adding further constraints such as the slope of S_{O2}. DSA could also be used to discover feature sets from signals of other sensors than dissolved oxygen. These feature sets could further improve the accuracy and robustness of an ammonium-depletion soft sensor or soft sensors for different quantities of interest.

We provide all the code under a GNU free public license in Carbajal and Schneider [44], hence readers can adapt it to their own analyses and for different models, as long as these models have the structure described in equation (3).

2.6 Limitations and outlook

As illustrated herein, DSA is applied to a specific model, and is restricted by the model's structure. For example, there is another known state variable that could cause a ramp: the alkalinity [45], which does not influence other states in the definition of ASM1. Hence, no DSA performed on ASM1 will inform us of the influence of alkalinity. However, the presented method for DSA can be applied to other models such as ASM3 to assess the relationship between alkalinity and the ramp feature. In the present work, it was decided to develop a proof of concept of the method based on ASM1 as this is still the most commonly used model in the ASM family.

DSA deals with deterministic dynamics, therefore process noise cannot be handled easily with the current approach. Measurement noise does not affect the dynamics, and therefore correlations between state variables and features based on them are not affected by measurement noise. Detection of these features in real systems, by means of sensors and state estimation, is however affected by measurement noise. Examining the impact of measurement noise and the feasibility of applying DSA results in practical applications is not the focus of this work, nor is it an inherent part of DSA analysis; these are additional analyses conducted subsequently.

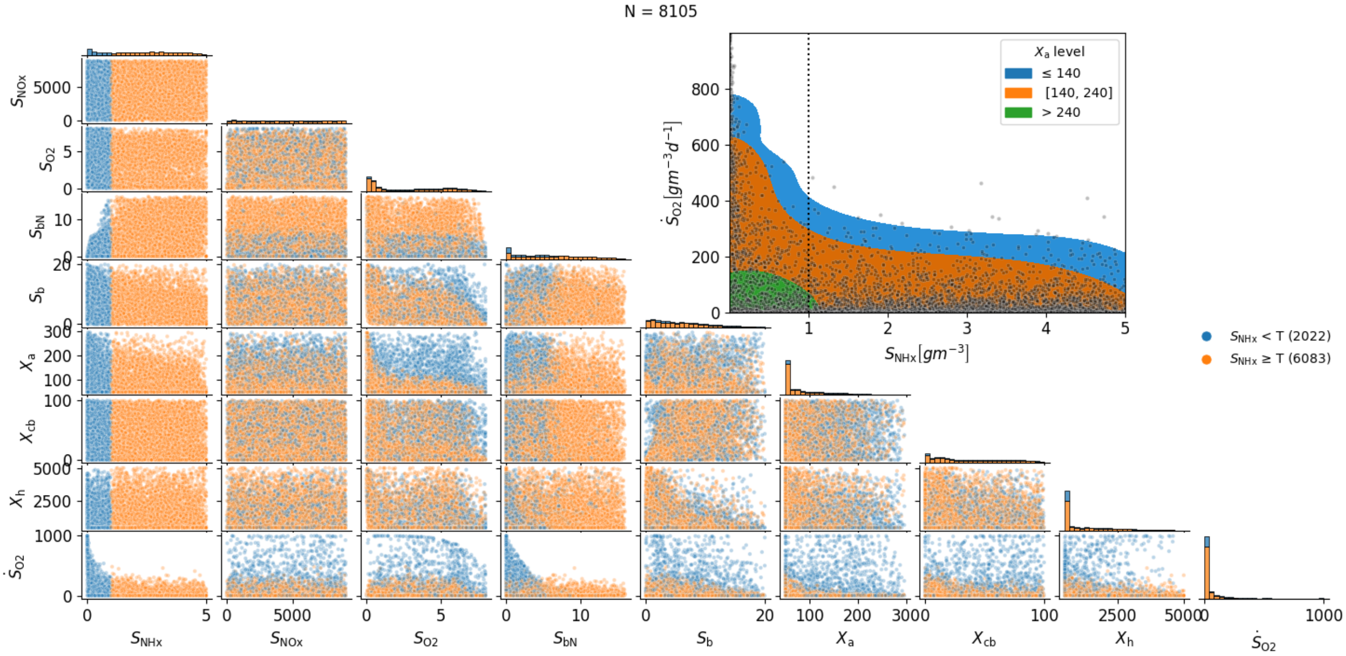

Figure 6: ASM1 ramp points distribution. Distribution of states fulfilling the ramp conditions (9) and (10). The points are colored by whether the value of S_{NHx} is above (orange) or below (blue) an arbitrary threshold (T). The number of samples (N) in each category is shown in the legend. The panels on the diagonal always show the density of points. The bottom row of the panels shows the value of the dissolved oxygen time derivative (ramp's slope). The top-right panel shows the relation between the ramp's slope and the ammonium concentration. The coloured regions on that panel show the level of autotrophic bacteria (X_{a}), illustrating a further correlation that can be exploited for increasing the accuracy of a full-ammonium-depletion detection soft sensor.

3 Conclusion

1. We used DSA to systematically evaluate all the mathematically possible solutions leading to a ramp feature in the dissolved oxygen signal in ASM1. The dissolved oxygen ramp is clearly immoral, meaning that not only a low value of the state S_{NHx}, i.e. an ammonium depletion, can cause the ramp feature, but also eight alternative causes, i.e. S_{O2}, S_{NOx}, S_{bN}, S_{b}, X_{a}, X_{cb}, X_{h}, X_{cbN}.
2. With DSA we identified that the slope of the dissolved oxygen at the locus of the ramp is relevant and can increase the accuracy of the ramp feature.
3. Many models (e.g. ASM family or ADM1) follow the same matrix structure which means that the formulae presented here can be applied "as-is" for a plethora of models in the water and resource recovery domain.
4. The analysis underlines how important systematic falsification studies are, especially when methods are developed for setups that can directly impact human and environmental health such as water recovery facilities for reuse purposes. With DSA, we suggest a concrete method for such a systematic analysis by increasing the robustness of soft sensors through the exposure of immoralities that can then be mitigated by multi-feature approaches.

4 Materials and methods

4.1 Dissolved oxygen feature

As introduced in section 1, a feature can be used to monitor a biochemical wastewater treatment process. From the two measurement signals pH and dissolved oxygen from a previous study [16], we here chose the latter, as S_{O2} is a state in the ASM1 while pH is not a state variable in any of the ASM models. This allowed us to start with a model with a small number (eight) of equations to implement. The feature of the dissolved oxygen is a ramp (see fig. 7) that can be used to predict the effluent ammonium (S_{NHx}) concentration. Olsson and Andrews [46] describe the ramp feature for a plug flow reactor, hence w.r.t. the location. Following the same principle in our study, we use an SBR, thus the ramp is w.r.t. time, i.e. whenever an inflection point is observed during the aeration phase, we assume that the ammonium is fully oxidised so the ammonium nitrogen is below or equal to an arbitrary threshold of $1\,\mathrm{g\,m^{-3}}$ [6]. If there is no ramp feature the effluent

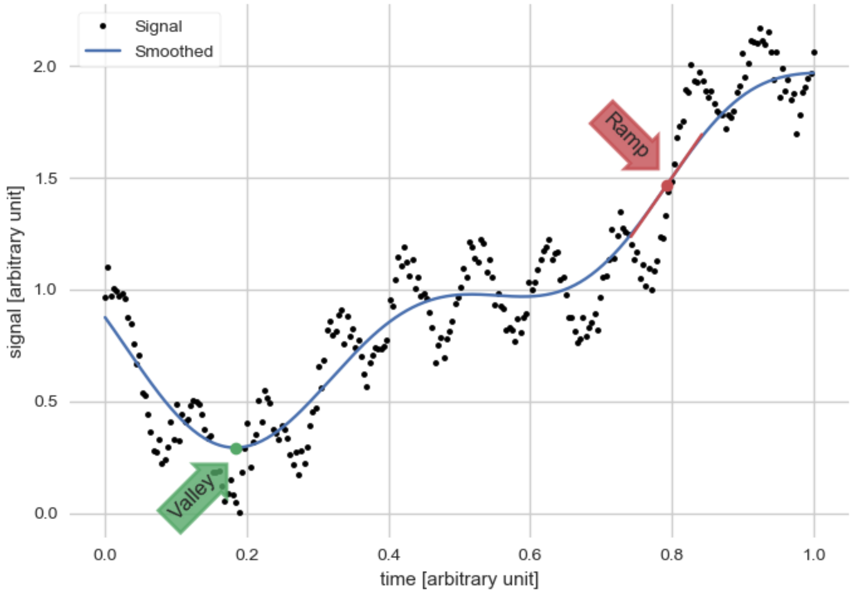

Figure 7: Illustration of two different features based on time derivatives of a signal. An extrema (valley) and a non-saddle inflection point (ramp). The latter we use in this article. An example for the arbitrary unit on the x-axis would be day on the y-axis it could be $\mathrm{g\,m^{-3}}$. The figure is created with Carbajal and Schneider [47].

ammonium concentration is estimated to be above $1\,\mathrm{g\,m^{-3}}$. For this prediction to be accurate and robust there should be no other state than an ammonium concentration below or equal to $1\,\mathrm{g\,m^{-3}}$ leading to the ramp feature. First, we obtain all the mathematically possible solutions for a ramp feature in ASM1 with DSA. See 4.2 for a detailed description of how we obtained these solutions. Next, we further constrain these mathematically possible solutions to the physically plausible ones by restricting them to only positive states. Restrictions were that concentrations cannot be negative and the setting of a wide, yet feasible range for all state variables. See tabs. 5-7 in the supplementary information for ranges reported in the literature, which we consulted to restrict the phase space of the state variables.

4.2 Model signal features

We are concerned with computing signal features based on the signal's derivatives w.r.t. time (time derivatives). Figure 7 shows two examples of such features: a valley, which is a minimum extreme point and a ramp. Extrema are zeros of the signal's first time derivative, and ramps are zeros of the second time derivative in which the first derivative is positive (i.e. non-saddle inflection point). The locus[1] of ramps can be described mathematically by (1).

Equation (1) can be used with signals that are differentiable twice. Also, we exclude saddle-points by requiring that the first time derivative is positive. The definition of ramp includes the concavity changing points of sigmoid functions like the hyperbolic tangent (as shown in fig. 7) and points at which the signal looks locally like a straight line (i.e. proportional to time), even if its concavity does not change sign.

Therefore, by obtaining an expression of the first and second time derivatives of the signal directly from the model, we can compute the locus of all ramps without solving the full differential equations or modelling time series.

4.3 Model structure

We apply our approach to models with the following structure:

$$\dot{\boldsymbol{x}} := \mathtt{M}\,\boldsymbol{r}(\boldsymbol{x}) + \boldsymbol{z} \tag{11}$$

$$\boldsymbol{y} := \boldsymbol{h}(\boldsymbol{x}) \tag{12}$$

where we used boldface, e.g. $\boldsymbol{x}$, for vectors, and capital typewriter font, e.g. $\mathtt{M}$ for matrices. In equation (11), $\boldsymbol{x}$ is the vector of states of the model, which herein we take to be a real column matrix, i.e. $\boldsymbol{x} \in \mathbb{R}^{N\times 1}$ (N is the number of states, e.g. $N = 13$ in the original ASM1, Henze et al. [39]). The states are then transformed via the mapping $\boldsymbol{r}(\boldsymbol{x})$, into a new vector, which herein we will call *rates* vector and, by slight abuse of notation, denote also $\boldsymbol{r}$. This transformation might not preserve

---

[1] set of all points that satisfies the specified conditions

the dimension, so the resulting rates vector might have a different dimension $\boldsymbol{r}(\boldsymbol{x}) \in \mathbb{R}^{R\times 1}$ (R is the number of reaction rates, e.g. $R = 8$ in the original ASM1, Henze et al. [39]).

The matrix $\mathtt{M}$ combines the R rates to produce the N time derivatives of the states, $\dot{\boldsymbol{x}}$. Hence we have $\mathtt{M} \in \mathbb{R}^{N\times R}$. The additional term ($\boldsymbol{z}$) in equation (11) represents the *actuation* on the states of the system[2].

Equation (12) (a.k.a. *measurement model* [48, ch. 4.3]) represents a mapping that generates measurement signals, $\boldsymbol{y}$ (modelling those that could be produced by a sensor), based on the model states ($\boldsymbol{x}$).

Until here we have omitted the dependence of equations (11)-(12) on parameters to keep the notation simple. All the model's components described till now can depend on parameters (free[3] and fundamental).

Many models for activated sludge and anaerobic digestion obey this structure, for example, all the ASM family [26], and several anaerobic digestions models [49] such as ADM1 [27]. As an example, all model components described above correspond to ASM1 and can be found in B.3, including tabs. 4 with all parameters and their description. This means that the mathematical analysis presented here can be applied to any model that follows the form in equations (11)-(12) by inserting the matrix and the rates of a different model than ASM1 into the formula.

As the model evolves in time, equation (11) provides the first time derivative of the signals. The second time derivative of all states is obtained by direct application of the chain rule:

$$\ddot{\boldsymbol{x}} = \mathtt{M}\,\dot{\boldsymbol{r}} + \dot{\boldsymbol{z}} = \mathtt{M}\,\mathtt{J}_{\boldsymbol{r}}\,\dot{\boldsymbol{x}} + \dot{\boldsymbol{z}} \tag{13}$$

where $\mathtt{J}_{\boldsymbol{r}}$ is the Jacobian of the rates w.r.t. the states, i.e.

$$\mathtt{J}_{\boldsymbol{r}} \coloneqq \begin{bmatrix} \nabla_{\boldsymbol{x}}^{\top} r_1(\boldsymbol{x}) \\ \vdots \\ \nabla_{\boldsymbol{x}}^{\top} r_R(\boldsymbol{x}) \end{bmatrix} = \begin{bmatrix} \partial_{x_1} r_1 & \dots & \partial_{x_N} r_1 \\ \vdots & \ddots & \vdots \\ \partial_{x_1} r_R & \dots & \partial_{x_N} r_R \end{bmatrix} \tag{14}$$

The ramps of the i-th signal in these models is then given by

$$\text{ramps} \coloneqq \{t : \mathtt{M}_{i,:}\,\boldsymbol{r} + z_i > 0 \wedge \mathtt{M}_{i,:}\,\mathtt{J}_{\boldsymbol{r}}\,\dot{\boldsymbol{x}} + \dot{z}_i = 0\} \tag{15}$$

4.4 Ramp contingency

Here the typical and the physical minimum and maximum values are presented for all eight relevant states that can cause the S_{O2} ramp feature.

For all the evaluations in this article, we used Python 3 [50] and SymPy [51] (any other computer algebra system could be used), complemented by a minimal amount of manual analysis that will be further automated in the future [44].

Data availability

All data supporting the findings of this study were generated using code available in the public GitLab repository at https://gitlab.com/sbrml/dsa-signal-features/. The repository contains all scripts and instructions necessary to reproduce the datasets and figures presented in this article in the folder doc/examples. The code is available under the GNU Public License Version 3, and can be accessed without restriction.

Acknowledgements

We are deeply grateful to Gustavo Buscaglia for the many insightful discussions and we thank Cyriel Carton for supporting the search for feasible state variable ranges.

Funding sources

MYS was supported by the Swiss National Science Foundation (P500PT_211132).

Authors contributions

MYS: Conceptualisation, Formal Analysis, Methodology, Funding Acquisition, Software, Validation, Visualisation, Writing - Original Draft, Review & Editing ET: Validation, Writing - Original Draft, Review & Editing JPC: Conceptualisation, Formal Analysis, Methodology, Software, Validation, Visualisation, Writing - Original Draft, Review & Editing

---

[2] The actuation might not be the inputs defined by a controller, a further *input model* ($\boldsymbol{b}$) might be needed: $\boldsymbol{z} \coloneqq \boldsymbol{b}(\boldsymbol{u})$, where $\boldsymbol{u}$ are the controllable inputs and $\boldsymbol{z}$ are the actuations

[3] parameters that must be estimated, e.g. experimentally

References

[1] Tove A Larsen, Sabine Hoffmann, Christoph Lüthi, Bernhard Truffer, and Max Maurer. Emerging solutions to the water challenges of an urbanizing world. *Science*, 352(6288):928–933, May 2016. doi: 10.1126/science.aad8641.

[2] Korneel Rabaey, Tom Vandekerckhove, Arjen Van de Walle, and David L. Sedlak. The third route: Using extreme decentralization to create resilient urban water systems. *Water Research*, 185:116276, October 2020. ISSN 0043-1354. doi: 10.1016/j.watres.2020.116276.

[3] Mark C. M. van Loosdrecht and Damir Brdjanovic. Anticipating the next century of wastewater treatment. *Science*, 344 (6191):1452–1453, June 2014. ISSN 0036-8075, 1095-9203. doi: 10.1126/science.1255183. Publisher: American Association for the Advancement of Science Section: Perspective.

[4] Sven Eggimann, Bernhard Truffer, Ulrike Feldmann, and Max Maurer. Screening European market potentials for small modular wastewater treatment systems – an inroad to sustainability transitions in urban water management? *Land Use Policy*, 78:711–725, November 2018. ISSN 0264-8377. doi: 10.1016/j.landusepol.2018.07.031.

[5] Henri Haimi, Michela Mulas, Francesco Corona, and Riku Vahala. Data-derived soft-sensors for biological wastewater treatment plants: An overview. *Environmental Modelling & Software*, 47:88–107, September 2013. doi: 10.1016/j.envsoft.2013.05.009.

[6] Mariane Yvonne Schneider, Viviane Furrer, Eleonora Sprenger, Juan Pablo Carbajal, Kris Villez, and Max Maurer. Benchmarking Soft Sensors for Remote Monitoring of On-Site Wastewater Treatment Plants. *Environmental Science & Technology*, 54(17):10840–10849, September 2020. ISSN 0013-936X, 1520-5851. doi: 10.1021/acs.est.9b07760.

[7] Hsiang-Yang Shyu, Cynthia J. Castro, Robert A. Bair, Qing Lu, and Daniel H. Yeh. Development of a Soft Sensor Using Machine Learning Algorithms for Predicting the Water Quality of an Onsite Wastewater Treatment System. *ACS Environmental Au*, June 2023. doi: 10.1021/acsenvironau.2c00072. Publisher: American Chemical Society.

[8] Siyuan Wang, Mariane Y. Schneider, Eveline I. P. Volcke, and Di Wu. How useful are data-driven methods for building-level greywater treatment from a process engineering perspective? *Water Research X*, page 100343, April 2025. ISSN 2589-9147. doi: 10.1016/j.wroa.2025.100343.

[9] J. Alferes, O. Grievson, C. Heffernan, D. Lumley, T. Massiri, A. Menniti, O. Samuelsson, K. Villez, and E. Zegers. Practical procedures for sensor quality assessment. In Kris Villez, Daniel Aguado, Janelcy Alferes, Queralt Plana, Maria Victoria Ruano, and Oscar Samuelsson, editors, *Metadata Collection and Organization in Wastewater Treatment and Wastewater Resource Recovery Systems*, pages 103–162. IWA Publishing, London, UK, June 2024. ISBN 978-1-78906-115-4. doi: 10.2166/9781789061154_0103.

[10] Francesca Cecconi, Samuel Reifsnyder, Reza Sobhani, Albert Cisquella-Serra, Marc Madou, and Diego Rosso. Functional behaviour and microscopic analysis of ammonium sensors subject to fouling in activated sludge processes. *Environmental Science: Water Research & Technology*, 6(10):2723–2733, 2020. ISSN 2053-1400, 2053-1419. doi: 10.1039/D0EW00359J.

[11] Oscar Samuelsson, Anders Björk, Jesús Zambrano, and Bengt Carlsson. Fault signatures and bias progression in dissolved oxygen sensors. *Water Science and Technology*, 78(5):1034–1044, October 2018. ISSN 0273-1223, 1996-9732. doi: 10.2166/wst.2018.350.

[12] Kito Ohmura, Christian M. Thürlimann, Marco Kipf, Juan Pablo Carbajal, and Kris Villez. Characterizing long-term wear and tear of ion-selective pH sensors. *Water Science and Technology*, 80(3):541–550, August 2019. ISSN 0273-1223, 1996-9732. doi: 10.2166/wst.2019.301.

[13] Heidi Lynn Ivan and Valentina Zaccaria. Exploring the effects of faults on the performance of a biological wastewater treatment process. *Water Science and Technology*, 90(2):474–489, June 2024. ISSN 0273-1223. doi: 10.2166/wst.2024.213.

[14] Bing Li, Siyuan Mao, Tuo Tian, Huaibin Bi, Yuxin Tian, Xueyan Ma, and Yong Qiu. Design and application of soft sensors in rural sewage treatment facilities. *AQUA - Water Infrastructure, Ecosystems and Society*, 72(11):2001–2016, November 2023. ISSN 2709-8028. doi: 10.2166/aqua.2023.062.

[15] Eva Reynaert, Philipp Steiner, Qixing Yu, Lukas D Olif, Noah Joller, Mariane Y. Schneider, and Eberhard Morgenroth. Predicting Microbial Water Quality in On-Site Water Reuse Systems with Online Sensors. *Water Research*, page 120075, May 2023. ISSN 0043-1354. doi: 10.1016/j.watres.2023.120075.

[16] Mariane Yvonne Schneider, Juan Pablo Carbajal, Viviane Furrer, Bettina Sterkele, Max Maurer, and Kris Villez. Beyond signal quality: The value of unmaintained pH, dissolved oxygen, and oxidation-reduction potential sensors for remote performance monitoring of on-site sequencing batch reactors. *Water Research*, 161:639–651, September 2019. ISSN 00431354. doi: 10.1016/j.watres.2019.06.007.

[17] Christian M. Thürlimann, Kai M. Udert, Eberhard Morgenroth, and Kris Villez. Stabilizing control of a urine nitrification process in the presence of sensor drift. *Water Research*, 165:114958, November 2019. ISSN 00431354. doi: 10.1016/j.watres.2019.114958.

[18] Dynamita. Sumo, 2019. URL https://www.dynamita.com.

[19] Fernando E. Rosas, Bernhard C. Geiger, Andrea I. Luppi, Anil K. Seth, Daniel Polani, Michael Gastpar, and Pedro A. M. Mediano. Software in the natural world: A computational approach to hierarchical emergence, June 2024. URL http://arxiv.org/abs/2402.09090. arXiv:2402.09090 [nlin].

[20] Steven Strogatz. *Nonlinear dynamics and chaos: with applications to physics, biology, chemistry, and engineering.* CRC Press, Boca Raton, third edition edition, 2024. ISBN 978-1-03-266521-4. OCLC: 1406021569.

[21] Nozomi Akashi, Yasuo Kuniyoshi, Taketomo Jo, Mitsuhiro Nishida, Ryo Sakurai, Yasumichi Wakao, and Kohei Nakajima. Embedding Bifurcations into Pneumatic Artificial Muscle. *Advanced Science*, 11(25):2304402, 2024. ISSN 2198-3844. doi: 10.1002/advs.202304402.

[22] J. P. Carbajal, Daniel A. Martin, and D. R. Chialvo. Learning by mistakes in memristor networks. *Physical Review E*, 105(5):054306, May 2022. doi: 10.1103/PhysRevE.105.054306. Publisher: American Physical Society.

[23] Ken Caluwaerts and Juan Pablo Carbajal. Energy conserving constant shape optimization of tensegrity structures. *International Journal of Solids and Structures*, 58:117–127, 2015. ISSN 00207683. doi: 10.1016/j.ijsolstr.2014.12.023. ISBN: 0020-7683.

[24] Sebastian Bathiany, Henk Dijkstra, Michel Crucifix, Vasilis Dakos, Victor Brovkin, Mark S. Williamson, Timothy M. Lenton, and Marten Scheffer. Beyond bifurcation: using complex models to understand and predict abrupt climate change. *Dynamics and Statistics of the Climate System*, 1(1):dzw004, January 2016. ISSN 2059-6987. doi: 10.1093/climsys/dzw004.

[25] György Haller. *Transport barriers and coherent structures in flow data: advective, diffusive, stochastic and active methods.* Cambridge university press, Cambridge, 2023. ISBN 978-1-00-922517-5.

[26] Mogens Henze, Willi Gujer, Takahashi Mino, and M. C. M. van Loosdrecht. *Activated sludge models ASM1, ASM2, ASM2d and ASM3.* IWA publishing. IWA, Londen, UK, 2000. ISBN 978-1-900222-24-2.

[27] D.J. Batstone, J. Keller, I. Angelidaki, S.V. Kalyuzhnyi, S.G. Pavlostathis, A. Rozzi, W.T.M. Sanders, H. Siegrist, and V.A. Vavilin. The IWA Anaerobic Digestion Model No 1 (ADM1). *Water Science and Technology*, 45(10):65–73, May 2002. ISSN 0273-1223, 1996-9732. doi: 10.2166/wst.2002.0292.

[28] P. A. Vanrolleghem. *On-line Modelling of Activated Sludge Processes: Development of an Adaptive Sensor.* Ph.D. thesis, Ghent Univeristy, Gent, Belgium, February 1994. URL https://modeleau.fsg.ulaval.ca/index.php?id=377.

[29] F. Grognard and O. Bernard. Stability analysis of a wastewater treatment plantwith saturated control. *Water Science and Technology*, 53(1):149–157, January 2006. ISSN 0273-1223. doi: 10.2166/wst.2006.017.

[30] Shuiwen Shen, Giuliano C. Premier, Alan Guwy, and Richard Dinsdale. Bifurcation and stability analysis of an anaerobic digestion model. *Nonlinear Dynamics*, 48(4):391–408, June 2007. ISSN 1573-269X. doi: 10.1007/s11071-006-9093-1.

[31] M. I. Nelson and H. S. Sidhu. Analysis of the activated sludge model (number 1). *Applied Mathematics Letters*, 22(5): 629–635, May 2009. ISSN 0893-9659. doi: 10.1016/j.aml.2008.05.003.

[32] E.I.P. Volcke, M. Sbarciog, E.J.L. Noldus, B. De Baets, and M. Loccufier. Steady state multiplicity of two-step biological conversion systems with general kinetics. *Mathematical Biosciences*, 228(2):160–170, December 2010. ISSN 00255564. doi: 10.1016/j.mbs.2010.09.004.

[33] B. Benyahia, T. Sari, B. Cherki, and J. Harmand. Bifurcation and stability analysis of a two step model for monitoring anaerobic digestion processes. *Journal of Process Control*, 22(6):1008–1019, July 2012. ISSN 0959-1524. doi: 10.1016/j.jprocont.2012.04.012.

[34] Astrid Bornhöft, Richard Hanke-Rauschenbach, and Kai Sundmacher. Steady-state analysis of the Anaerobic Digestion Model No. 1 (ADM1). *Nonlinear Dynamics*, 73(1):535–549, July 2013. ISSN 1573-269X. doi: 10.1007/s11071-013-0807-x.

[35] Davide Dionisi, Adamu A. Rasheed, and Aniruddha Majumder. A new method to calculate the periodic steady state of sequencing batch reactors for biological wastewater treatment: Model development and applications. *Journal of Environmental Chemical Engineering*, 4(3):3665–3680, September 2016. ISSN 2213-3437. doi: 10.1016/j.jece.2016.07.032.

[36] Matthew J. Wade and Gail S. K. Wolkowicz. Bifurcation Analysis of an Impulsive System Describing Partial Nitritation and Anammox in a Hybrid Reactor. *Environmental Science & Technology*, 55(3):2099–2109, February 2021. ISSN 0013-936X. doi: 10.1021/acs.est.0c06275. Publisher: American Chemical Society.

[37] Otacílio B. L. Neto, Michela Mulas, and Francesco Corona. About the classical and structural controllability and observability of a common class of activated sludge plants. *Journal of Process Control*, 111:8–26, March 2022. ISSN 0959-1524. doi: 10.1016/j.jprocont.2021.12.013.

[38] Emmanuel Sampaio, Michela Mulas, Otacílio Neto, and Francesco Corona. Structural analysis of an activated sludge process with greenhouse gas emissions, November 2022.

[39] M. Henze, C. P. Leslie Grady, W. Gujer, G. V. R. Marais, and T. Matsuo. A general model for single-sludge wastewater treatment systems. *Water Research*, 21(5):505–515, May 1987. ISSN 0043-1354. doi: 10.1016/0043-1354(87)90058-3.

[40] H. Hauduc, L. Rieger, I. Takács, A. Héduit, P. A. Vanrolleghem, and S. Gillot. A systematic approach for model verification: application on seven published activated sludge models. *Water Science and Technology*, 61(4):825–839, February 2010. ISSN 0273-1223. doi: 10.2166/wst.2010.898. _eprint: https://iwaponline.com/wst/article-pdf/61/4/825/1044907/825.pdf.

[41] Mariane Yvonne Schneider, Ward Quaghebeur, Sina Borzooei, Andreas Froemelt, Feiyi Li, Ramesh Saagi, Matthew J. Wade, Jun-Jie Zhu, and Elena Torfs. Hybrid modelling of water resource recovery facilities: status and opportunities. *Water Science and Technology*, 85(9):2503–2524, April 2022. ISSN 0273-1223. doi: 10.2166/wst.2022.115.

[42] Willi Gujer and Mogens Henze. Activated Sludge Modelling and Simulation. *Water Science and Technology*, 23:1011–1023, February 1991. doi: 10.2166/wst.1991.0553.

[43] J Pearl and D Mackenzie. *The Book of Why: The New Science of Cause and Effect*. Penguin Books Limited, 2018. ISBN 978-0-241-24264-3.

[44] Juan Pablo Carbajal and Mariane Yvonne Schneider. dynamical systems analysis, 2024. URL `https://gitlab.com/sbrml/dsa-signal-features/`.

[45] Ibrahim A. Al-Ghusain, Jason Huang, Oliver J. Hao, and Bong S. Lim. Using pH as a real-time control parameter for wastewater treatment and sludge digestion processes. *Water Science and Technology*, 30(4):159–168, 1994. doi: 10.2166/wst.1994.0182.

[46] G. Olsson and J. F. Andrews. The dissolved oxygen profile—A valuable tool for control of the activated sludge process. *Water Research*, 12(11):985–1004, January 1978. ISSN 0043-1354. doi: 10.1016/0043-1354(78)90082-9.

[47] Juan Pablo Carbajal and Mariane Yvonne Schneider. SBR features, 2019. URL `https://sbrml.gitlab.io/sbrfeatures/`.

[48] Lennart Ljung. *System identification: theory for the user*. Prentice Hall PTR, 2nd editio edition, 1999. ISBN 978-0-13-656695-3.

[49] Karthik R. Manchala, Yewei Sun, Dian Zhang, and Zhi-Wu Wang. Anaerobic Digestion Modelling. In *Advances in Bioenergy*, volume 2, pages 69–141. Elsevier, 2017. ISBN 978-0-12-812286-0. doi: 10.1016/bs.aibe.2017.01.001.

[50] Guido Van Rossum and Fred L. Drake. *Python 3 Reference Manual*. CreateSpace, Scotts Valley, CA, 2009. ISBN 1441412697.

[51] Aaron Meurer, Christopher P. Smith, Mateusz Paprocki, Ondřej Čertík, Sergey B. Kirpichev, Matthew Rocklin, Amit Kumar, Sergiu Ivanov, Jason K. Moore, Sartaj Singh, Thilina Rathnayake, Sean Vig, Brian E. Granger, Richard P. Muller, Francesco Bonazzi, Harsh Gupta, Shivam Vats, Fredrik Johansson, Fabian Pedregosa, Matthew J. Curry, Andy R. Terrel, Štěpán Roučka, Ashutosh Saboo, Isuru Fernando, Sumith Kulal, Robert Cimrman, and Anthony Scopatz. Sympy: symbolic computing in python. *PeerJ Computer Science*, 3:e103, January 2017. ISSN 2376-5992. doi: 10.7717/peerj-cs.103.

[52] J. Alex, L. Benedetti, J. Copp, K.V. Gernaey, Ulf Jeppsson, I. Nopens, M.-N. Pons, J.-P. Steyer, and P.A. Vanrolleghem. *Benchmark Simulation Model no. 1 (BSM1)*, volume TEIE-7229. Lund University, 2008.

[53] Patcharin Racho and Apinya Pongampornnara. Enhanced biogas production from modified tapioca starch wastewater. *Energy Reports*, 6:744–750, 2020. ISSN 2352-4847. doi: https://doi.org/10.1016/j.egyr.2019.09.058.

[54] Thomas Dockhorn, Joerg Felmeden, Thomas Hillenbrand, I Kaufmann Alves, Bernd Kirschbaum, Guenter Langergraber, Sabine Lautenschlaeger, Max Maurer, Silke Neuhausen, Julia Sigglow, and Heidrun Steinmetz. *Arbeitsblatt DWA-A 272 Grundsätze für die Planung und Implementierung Neuartiger Sanitärsysteme (NASS)*. DWA-Regelwerk. DWA, Hennef, Germany, first edition, June 2014. ISBN 978-3-944328-63-8.

[55] Seow Wah How, Jia Huey Sin, Sharon Ying Ying Wong, Pek Boon Lim, Alijah Mohd Aris, Gek Cheng Ngoh, Tadashi Shoji, Thomas P. Curtis, and Adeline Seak May Chua. Characterization of slowly-biodegradable organic compounds and hydrolysis kinetics in tropical wastewater for biological nitrogen removal. *Water Science and Technology*, 81(1):71–80, February 2020. ISSN 0273-1223. doi: 10.2166/wst.2020.077.

[56] Kathryn S Lowe, Maria B Tucholke, Jill M.B Tomaras, Kathleen Conn, Christiane Hoppe, Jörg E Drewes, John E McCray, and Junko Munakata-Marr. Influent Constituent Characteristics of the Modern Waste Stream from Single Sources: Final Report, September 2009. URL `http://web.archive.org/web/20190216024758/http://www.decentralizedwater.org/research_project_04-DEC-1.asp`.

[57] Pradip B. Dhamole, Rashmi R. Nair, Stanislaus F. D'Souza, and S. S. Lele. Denitrification of high strength nitrate waste. *Bioresource Technology*, 98(2):247–252, January 2007. ISSN 0960-8524. doi: 10.1016/j.biortech.2006.01.019.

[58] Shifa Zhong, Kai Zhang, Majid Bagheri, Joel G. Burken, April Gu, Baikun Li, Xingmao Ma, Babetta L. Marrone, Zhiyong Jason Ren, Joshua Schrier, Wei Shi, Haoyue Tan, Tianbao Wang, Xu Wang, Bryan M. Wong, Xusheng Xiao, Xiong Yu, Jun-Jie Zhu, and Huichun Zhang. Machine Learning: New Ideas and Tools in Environmental Science and Engineering. *Environmental Science & Technology*, 55(19):12741–12754, October 2021. ISSN 0013-936X. doi: 10.1021/acs.est.1c01339. Publisher: American Chemical Society.

A Supplementary information

A.1 Time derivatives

Here we detail the calculation for the time derivative of a model with the following structure

$$\dot{\boldsymbol{x}} = \mathtt{M}\boldsymbol{r}(\boldsymbol{x}) \tag{16}$$

to which we introduce a new term in the derivatives

$$\dot{\boldsymbol{x}} = \mathtt{M}\boldsymbol{r}(\boldsymbol{x}) + \boldsymbol{z}(\boldsymbol{x}, t) \tag{17}$$

By direct derivation, the second time derivative reads (we do not show the explicit dependence anymore):

$$\ddot{\boldsymbol{x}} = \mathtt{M}\dot{\boldsymbol{r}} + \dot{\boldsymbol{z}} \tag{18}$$

$$\dot{\boldsymbol{r}} = \partial_{\boldsymbol{x}}\boldsymbol{r}\;\dot{\boldsymbol{x}} \tag{19}$$

$$\dot{\boldsymbol{z}} = \partial_{\boldsymbol{x}}\boldsymbol{z}\;\dot{\boldsymbol{x}} + \partial_t\boldsymbol{z} \tag{20}$$

replacing

$$\ddot{\boldsymbol{x}} = \mathtt{M}\partial_{\boldsymbol{x}}\boldsymbol{r}\;\dot{\boldsymbol{x}} + \partial_{\boldsymbol{x}}\boldsymbol{z}\;\dot{\boldsymbol{x}} + \partial_t\boldsymbol{z} \tag{21}$$

Another approach is to think that the introduction of the derivatives modifies the structure of the system in (16):

$$\dot{\boldsymbol{x}} = \mathtt{M}^*\boldsymbol{r}^*(\boldsymbol{x}) \tag{22}$$

with the new elements being concatenations of the old

$$\mathtt{M}^* = \begin{bmatrix}\mathtt{M} & \mathbb{I}_{\dim \boldsymbol{z}}\end{bmatrix} \tag{23}$$

$$\boldsymbol{r}^*(\boldsymbol{x}) = \begin{bmatrix}\boldsymbol{r}(\boldsymbol{x}) \\ \boldsymbol{z}(\boldsymbol{x}, t)\end{bmatrix} \tag{24}$$

where $\mathbb{I}_{\dim \boldsymbol{z}}$ is the identity matrix of the size of $\boldsymbol{z}$. Expanding:

$$\mathtt{M}^*\boldsymbol{r}^* = \begin{bmatrix}\mathtt{M} & \mathbb{I}_{\dim \boldsymbol{z}}\end{bmatrix}\begin{bmatrix}\boldsymbol{r} \\ \boldsymbol{z}\end{bmatrix} = \mathtt{M}\boldsymbol{r} + \boldsymbol{z} \tag{25}$$

which shows the equivalence to eq. (17). In this case the second derivative is,

$$\ddot{\boldsymbol{x}} = \mathtt{M}^*\dot{\boldsymbol{r}}^* = \mathtt{M}^*\left(\partial_{\boldsymbol{x}}\boldsymbol{r}^*\;\dot{\boldsymbol{x}} + \partial_t\boldsymbol{r}^*\right) \tag{26}$$

which gives a simple general formula applicable also in the absence of actuation.

To verify equality with the previous derivation we expand the terms. Computing the Jacobian

$$\partial_{\boldsymbol{x}}\boldsymbol{r}^* = \partial_{\boldsymbol{x}}\begin{bmatrix}\boldsymbol{r} \\ \boldsymbol{z}\end{bmatrix} = \begin{bmatrix}\partial_{\boldsymbol{x}}\boldsymbol{r} \\ \partial_{\boldsymbol{x}}\boldsymbol{z}\end{bmatrix} \tag{27}$$

then

$$\partial_{\boldsymbol{x}}\boldsymbol{r}^*\;\dot{\boldsymbol{x}} = \begin{bmatrix}\partial_{\boldsymbol{x}}\boldsymbol{r} \\ \partial_{\boldsymbol{x}}\boldsymbol{z}\end{bmatrix}\dot{\boldsymbol{x}} = \begin{bmatrix}\partial_{\boldsymbol{x}}\boldsymbol{r}\;\dot{\boldsymbol{x}} \\ \partial_{\boldsymbol{x}}\boldsymbol{z}\;\dot{\boldsymbol{x}}\end{bmatrix} \tag{28}$$

and

$$\mathtt{M}^*\partial_{\boldsymbol{x}}\boldsymbol{r}^*\;\dot{\boldsymbol{x}} = \begin{bmatrix}\mathtt{M} & \mathbb{I}_{\dim \boldsymbol{z}}\end{bmatrix}\begin{bmatrix}\partial_{\boldsymbol{x}}\boldsymbol{r}\;\dot{\boldsymbol{x}} \\ \partial_{\boldsymbol{x}}\boldsymbol{z}\;\dot{\boldsymbol{x}}\end{bmatrix} = M\partial_{\boldsymbol{x}}\boldsymbol{r}\;\dot{\boldsymbol{x}} + \partial_{\boldsymbol{x}}\boldsymbol{z}\;\dot{\boldsymbol{x}} \tag{29}$$

The temporal term is

$$\mathtt{M}^*\partial_t\boldsymbol{r}^* = \begin{bmatrix}\mathtt{M} & \mathbb{I}_{\dim \boldsymbol{z}}\end{bmatrix}\begin{bmatrix}\partial_t\boldsymbol{r} \\ \partial_t\boldsymbol{z}\end{bmatrix} = \mathtt{M}\overbrace{\partial_t\boldsymbol{r}}^{\mathbf{0}} + \partial_t\boldsymbol{z} \tag{30}$$

Putting all together

$$\ddot{\boldsymbol{x}} = M\partial_{\boldsymbol{x}}\boldsymbol{r}\;\dot{\boldsymbol{x}} + \partial_{\boldsymbol{x}}\boldsymbol{z}\;\dot{\boldsymbol{x}} + \partial_t\boldsymbol{z} \tag{31}$$

which is the same as eq. (21).

A.1.1 Single state actuation

If we assume that the actuation does not depend directly on time, and only depends in a single state, the actuation vector has the form:

$$\boldsymbol{z}(\boldsymbol{x}, t) = \mathbf{1}_{x_i} z(x_i) \tag{32}$$

where $\mathbf{1}_{x_i}$ is a column vector filled with zeros, except in the location of element x_i. That is, $\boldsymbol{z}$ affects only the state x_i and it depends only on that state.

We have that

$$\partial_t \boldsymbol{z} = \mathbf{0} \tag{33}$$

$$\partial_{\boldsymbol{x}} \boldsymbol{z}\, \dot{\boldsymbol{x}} = \partial_{\boldsymbol{x}} \mathbf{1}_{x_i} z(x_i)\, \dot{\boldsymbol{x}} = \partial_{x_i} z\ \mathbb{1}_{x_i x_i} \dot{\boldsymbol{x}} = \partial_{x_i} z\ \dot{x}_i\ \mathbf{1}_{x_i} \tag{34}$$

where $\mathbb{1}_{x_i x_i}$ is a matrix with a 1 in the (x_i, x_i) element, and zero otherwise. By replacing into eq. (31) we obtain,

$$\ddot{\boldsymbol{x}} = M \partial_{\boldsymbol{x}} \boldsymbol{r}\ \dot{\boldsymbol{x}} + \partial_{x_i} z\ \dot{x}_i\ \mathbf{1}_{x_i} \tag{35}$$

and the x_i component is

$$\ddot{x}_i = M_{x_i:} \partial_{\boldsymbol{x}} \boldsymbol{r}\ \dot{\boldsymbol{x}} + \partial_{x_i} z\ \dot{x}_i \tag{36}$$

These are the formulas used in the software [44] accompanying this publication.

B Ramp points curve

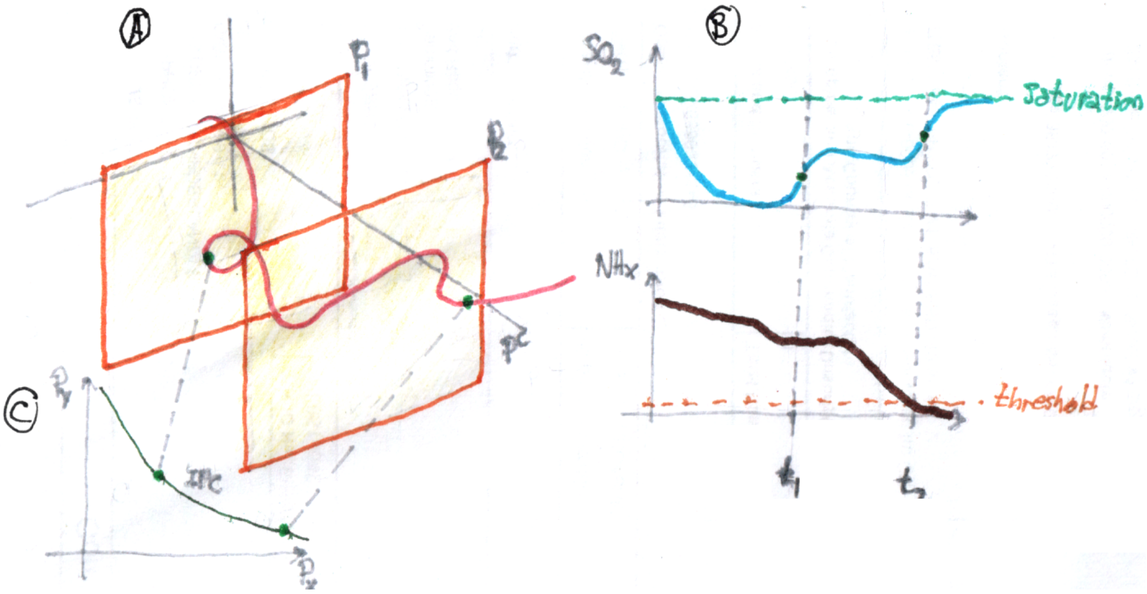

Figure 8: Construction and interpretation of a ramp points curve. A: a trajectory of a dynamical system in $\mathbb{R}^N$. In the drawing, the space is decomposed in two sub-spaces of dimension 2 (the planes are labelled with P in the diagram), and $N-2$ (the perpendicular direction to the planes, the orthogonal complement $P^{\perp}$ of P). By fixing the values of all components of a vector in $P^{\perp}$ a plane is defined as shown. The trajectory crosses these planes as it evolves. B: Components of the trajectory can be plotted as a function of time, as an example the states S_{O2} and NH_x from ASM1 are shown. The points in which a ramp is realised are marked here and in the trajectory. The time of the ramps have their corresponding planes in panel A, t_1 with P_1, etc. C: By merging all the planes and the points corresponding to a ramp in them, we obtain the locus of all ramps. These loci might look like curves in the obtained plot. The curve collects points from different planes (different values of the states in $P^{\perp}$)

The locus of all ramps defines a hyper-surface of dimension $\mathbb{R}^{N-1}$. This surface cannot be visualized easily. Therefore we choose a sub-space of dimension 2 that we call P (for plane) and we collect points fulfilling the ramp conditions in it.

In P we have two states of our choice, e.g. S_{O2} and X_{a}, and all other states are in the orthogonal complement of P, called $P^{\perp}$. In fig. 8 we depict $P^{\perp}$ as a single direction, but the reader should understand that in fact, this sub-space is of dimension $N-2$.

Figure 9: Multiple trajectories crossing the plane P, for fixed values of $P^{\perp}$. Some trajectories intersect the plane with a ramp in the time signal of the selected component, e.g. S_{O2}, while others do not (pink trajectory). Only those with a ramp contribute to the ramp locus (dashed lines on P).

To put a ramp point in P, we must first define a value for all states in $P^{\perp}$. These are the planes shown in panel A of fig. 8. For any value we choose for these other states, and for any value of the states in P, we can always find a trajectory of the dynamical system that goes through the point in the full space. Hence, the reader should imagine each of these planes crossed by many trajectories as the ones shown here, each one intersecting the plane at a unique point. We then filter the intersection points by selecting those that fulfil the ramp condition. Then we repeat this process for different values of the states in $P^{\perp}$ (different planes in the figure). We collect all these points in a single plane. These are the curves shown in fig. 5 in the body of the article.

The points shown in fig. 6 are obtained in a similar fashion. However, for these points, we do not fix any state. All states (including S_{NHx}) are free, and to sample the hyper-surface defined by the ramp conditions (9) and (10), we solve an optimisation problem, which can be stated as follows: generate distinct points in a level set defined by a function $\phi : \mathbb{R}^n \to \mathbb{R}$ (in our case $n = 8$):

$$\mathscr{L}_c := \{x \in \mathbb{R}^n : \phi(x) = c\} \tag{37}$$

To warrant good behaviour of the set, we assume that the function has the following properties:

1. is continuous: implies closedness of the sets $\{x \in \mathbb{R}^n : \phi(x) \leq c\}$ (sublevel set)
2. $\nabla\phi(x) \neq 0 \quad \forall x \in \mathscr{L}_c$ (non-degenerate level set, level sets do nott intersect)
3. is coercive: $\lim_{\|x\|\to\infty} \phi(x) = \infty$ (compact sublevel sets). That is: ϕ is coercive $\iff$ $\forall c \in \mathbb{R}$, $\{x \in \mathbb{R}^n : \phi(x) \leq c\}$ is compact.

We can set the problem of sampling the ramp hyper-surface as a constrained optimization:

$$x = \underset{x \in S \subset \mathbb{R}^n}{\arg\min}\, f(x, \theta) \tag{38}$$

$$\phi(x) = 0 \quad \text{eq. } (9) \tag{39}$$

$$\psi(x) > 0 \quad \text{eq. } (10) \tag{40}$$

where S is chosen such that $\mathscr{L}_c \cap S \neq \emptyset$ (e.g. a hyperbox), and the cost function $f(x) : \mathbb{R}^n \to \mathbb{R}$ is arbitrary. The quality of the optimization results for our sampling can be verified by looking at the distributions shown in fig. 10. There the values of $\phi(x)$ are shown (second time derivative, which should be zero), together with the values of $\psi(x)$ (first time derivative, must be positive).

The cost function is exploited to achieve other objectives, like the spread of the points over the surface. For example:

$$f(x, \{x_i\}_{1\leq i \leq I}, r_{\min}) = -\sum_{i=1}^{I} H(r_{\min} - \|x - x_i\|)\|x - x_i\|^2 \tag{41}$$

where $\{x_i\}_{1\leq i\leq I}$ is a set of points in $\mathscr{L}_c$ (e.g. the set of previous solutions to the problem). $H(r)$ is the step function, with value 1 when $r > 0$.

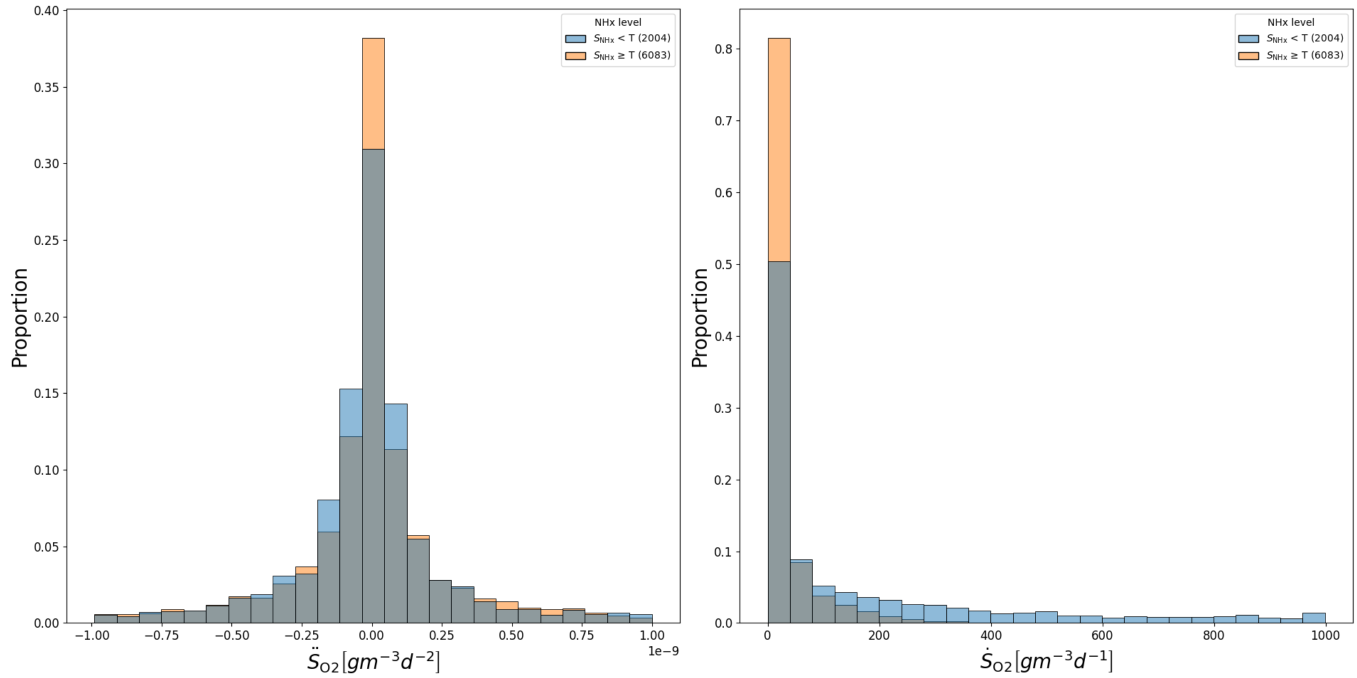

Figure 10: Values of the dissolved oxygen time derivatives of the selected samples from fig. 6

Numerical solutions using Sequential Quadratic Programming (SQP) showed an accumulation of solutions on the boundary of the intersection $\mathscr{L}_c \cap S$, likely due to the Karush–Kuhn–Tucker conditions. Other constrained optimizers are to be tested, but as a workaround, the cost function can be extended to

$$\tilde{f}(x, \{x_i\}_{1\leq i\leq I}, \partial S) = f(x, \{x_i\}_{1\leq i\leq I}) + \text{spike}(x, \partial S) \tag{42}$$

where spike is a function that increases rapidly as x approaches the boundary (∂S) of S. This workaround and a very tight hyperbox provided the results reported.

B.1 Interpretability of the inflection point curve

Figure 11 is the result from an interactive plot where points in the $(X_\text{h}, S_\text{O2})$ plane can be selected and the time-series are reproduced from these points. The point on the blue line in the top figures are ramps, the points away from the curve or instances where no ramp occurs. From these points then the dissolved oxygen signals are reconstructed. This illustrates the simulation time that we save by computing the inflection point curve directly. Hence, we evaluated ramps for 100,000 initial conditions in a few minutes on a normal laptop, which covers a large region of the state-space.

B.2 Symbols name

B.3 ASM1 model

$$\boldsymbol{x} = \begin{bmatrix} S_\text{nb} \\ S_\text{b} \\ X_\text{nb,in} \\ X_\text{cb} \\ X_\text{h} \\ X_\text{a} \\ X_\text{nb,e} \\ S_\text{O2} \\ S_\text{NOx} \\ S_\text{NHx} \\ S_\text{bN} \\ X_\text{cbN} \\ S_\text{alk} \\ S_\text{N2} \end{bmatrix} \tag{43}$$

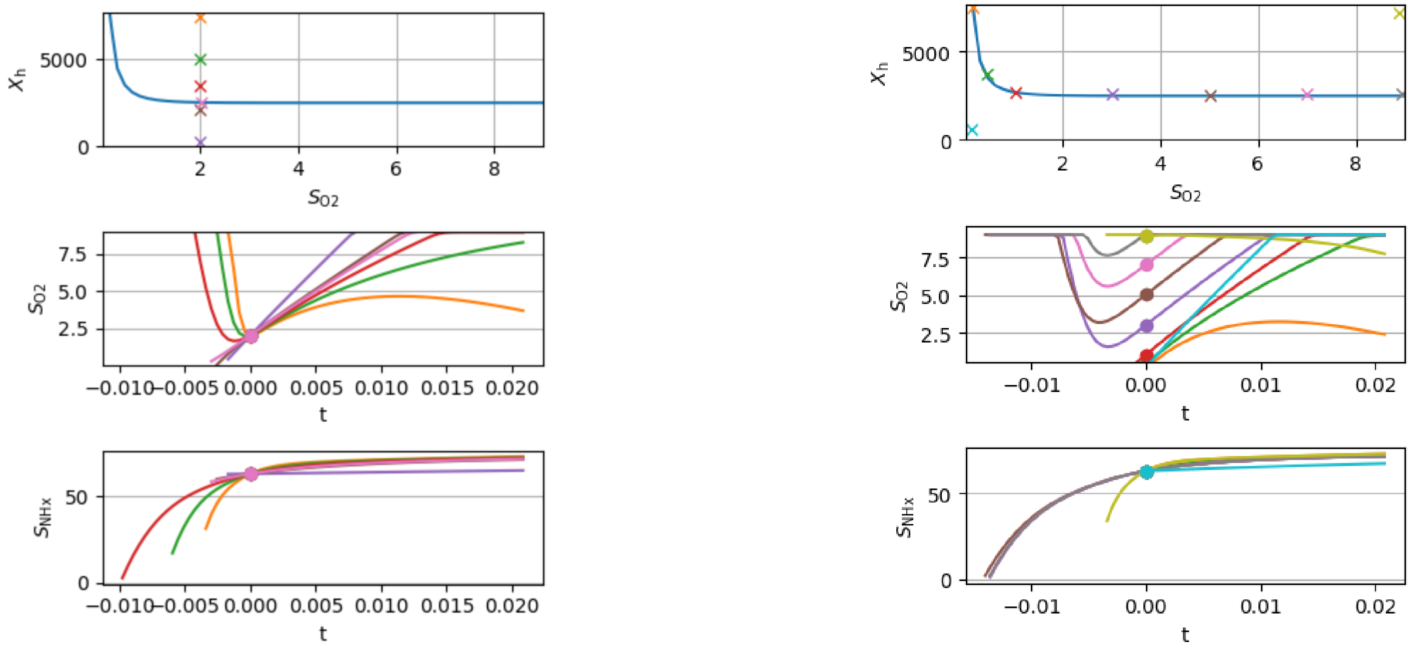

(a) Reconstruction for $S_{O2} = 2\,\mathrm{g\,m^{-3}}$.

(b) Reconstruction along the inflection point curve.

Figure 11: Reconstruction of the S_{O2} and S_{NHx} curve from selected points, marked with an x, in the S_{O2}, X_h plane. In a) only one value is on the inflection point curve, hence has a ramp, in b) all but the two in the bottom left and upper right corner are combinations of states with ammonium above the threshold leading to ramps.

This work	Other name	Description
S_b	S_B	Soluble biodegradable organics (SS)
S_{nb}	S_U	Soluble nondegradable organics (SI)
S_{O2}	S_{O2}	Dissolved oxygen (SO)
X_{cb}	XC_B	Particulate and colloidal biodegradable organics (XS)
$X_{nb,in}$	X_{UInf}	Particulate nonbiodegradable organics from the influent (XI)
$X_{nb,e}$	X_{UE}	Particulate nonbiodegradable endogenous products (XP)
S_{NHx}	S_{NHx}	Ammonia (NH4 + NH3) (SNH)
S_{NOx}	S_{NOx}	Nitrate and nitrite (NO3 + NO2) (considered to be NO3 only for stoichiometry, SNO)
X_{cbN}	XC_{BN}	Particulate and colloidal biodegradable organic N (XND)
S_{bN}	S_{BN}	Soluble biodegradable organic N (SND)
X_h	X_{OHO}	Ordinary heterotrophic organisms(XBH)
X_a	X_{ANO}	Autotrophic nitrifying organisms (NH4+ to NO3-, XBA)
S_{alk}	S_{Alk}	Alkalinity (HCO3-, SALK)
S_{N2}	S_{N2}	Dissolved nitrogen (gas, N2), not in classic ASM1

Table 2: Naming of states in this work in relation to commonly used names, e.g. [26], which is provided in the bracket in the description. The "other name" column is based on [40].

This work	Other name	Description
g_{hO2}	g_{hO2}	Aerobic growth of heterotrophs
g_{hAn}	g_{hAn}	Anoxic growth of heterotrophs
g_{aO2}	g_{aO2}	Aerobic growth of autotrophs
d_h	d_h	Decay of heterotrophs
d_a	d_a	Decay of autotrophs
a_N	am_N	Ammonification of soluble organic nitrogen
h_o	ho	Hydrolysis of entrapped organics
h_{oN}	ho_N	Hydrolysis of entrapped organic nitrogen

Table 3: Naming of process rates and their description. The "other name" column is following [40].

$$\mathtt{M} = \begin{bmatrix} 0 & 0 & 0 & 0 & 0 & 0 & 0 & 0 \\ m_{S_{\mathrm{b}}\,g_{\mathrm{hO2}}} & m_{S_{\mathrm{b}}\,g_{\mathrm{hAn}}} & 0 & 0 & 0 & 0 & 1 & 0 \\ 0 & 0 & 0 & 0 & 0 & 0 & 0 & 0 \\ 0 & 0 & 0 & m_{X_{\mathrm{cb}}\,d_{\mathrm{h}}} & m_{X_{\mathrm{cb}}\,d_{\mathrm{a}}} & 0 & -1 & 0 \\ 1 & 1 & 0 & -1 & 0 & 0 & 0 & 0 \\ 0 & 0 & 1 & 0 & -1 & 0 & 0 & 0 \\ 0 & 0 & 0 & m_{X_{\mathrm{nb,e}}\,d_{\mathrm{h}}} & m_{X_{\mathrm{nb,e}}\,d_{\mathrm{a}}} & 0 & 0 & 0 \\ m_{S_{\mathrm{O2}}\,g_{\mathrm{hO2}}} & 0 & m_{S_{\mathrm{O2}}\,g_{\mathrm{aO2}}} & 0 & 0 & 0 & 0 & 0 \\ 0 & m_{S_{\mathrm{NOx}}\,g_{\mathrm{hAn}}} & m_{S_{\mathrm{NOx}}\,g_{\mathrm{aO2}}} & 0 & 0 & 0 & 0 & 0 \\ m_{S_{\mathrm{NHx}}\,g_{\mathrm{hO2}}} & m_{S_{\mathrm{NHx}}\,g_{\mathrm{hAn}}} & m_{S_{\mathrm{NHx}}\,g_{\mathrm{aO2}}} & 0 & 0 & 1 & 0 & 0 \\ 0 & 0 & 0 & 0 & 0 & -1 & 0 & 1 \\ 0 & 0 & 0 & m_{X_{\mathrm{cbN}}\,d_{\mathrm{h}}} & m_{X_{\mathrm{cbN}}\,d_{\mathrm{a}}} & 0 & 0 & -1 \\ m_{S_{\mathrm{alk}}\,g_{\mathrm{hO2}}} & m_{S_{\mathrm{alk}}\,g_{\mathrm{hAn}}} & m_{S_{\mathrm{alk}}\,g_{\mathrm{aO2}}} & 0 & 0 & m_{S_{\mathrm{alk}}\,a_{\mathrm{N}}} & 0 & 0 \\ 0 & m_{S_{\mathrm{N2}}\,g_{\mathrm{hAn}}} & 0 & 0 & 0 & 0 & 0 & 0 \end{bmatrix} \tag{44}$$

$$m_{S_{\mathrm{b}}\,g_{\mathrm{hO2}}} \coloneqq -\frac{1}{\gamma_{\mathrm{h}}} \tag{45}$$

$$m_{S_{\mathrm{b}}\,g_{\mathrm{hAn}}} \coloneqq -\frac{1}{\gamma_{\mathrm{h}}} \tag{46}$$

$$m_{X_{\mathrm{cb}}\,d_{\mathrm{h}}} \coloneqq 1 - \zeta_{\mathrm{Xnb,l}} \tag{47}$$

$$m_{X_{\mathrm{cb}}\,d_{\mathrm{a}}} \coloneqq 1 - \zeta_{\mathrm{Xnb,l}} \tag{48}$$

$$m_{X_{\mathrm{nb,e}}\,d_{\mathrm{h}}} \coloneqq \zeta_{\mathrm{Xnb,l}} \tag{49}$$

$$m_{X_{\mathrm{nb,e}}\,d_{\mathrm{a}}} \coloneqq \zeta_{\mathrm{Xnb,l}} \tag{50}$$

$$m_{S_{\mathrm{O2}}\,g_{\mathrm{hO2}}} \coloneqq \frac{\gamma_{\mathrm{h}} - 1}{\gamma_{\mathrm{h}}} \tag{51}$$

$$m_{S_{\mathrm{O2}}\,g_{\mathrm{aO2}}} \coloneqq \frac{\gamma_{\mathrm{a}} + \iota_{\mathrm{COD,NO3}}}{\gamma_{\mathrm{a}}} \tag{52}$$

$$m_{S_{\mathrm{NOx}}\,g_{\mathrm{hAn}}} \coloneqq \frac{\gamma_{\mathrm{h}} - 1}{\gamma_{\mathrm{h}}\iota_{\mathrm{NO3,N2}}} \tag{53}$$

$$m_{S_{\mathrm{NOx}}\,g_{\mathrm{aO2}}} \coloneqq \frac{1}{\gamma_{\mathrm{a}}} \tag{54}$$

$$m_{S_{\mathrm{NHx}}\,g_{\mathrm{hO2}}} \coloneqq -\iota_{\mathrm{NXb}} \tag{55}$$

$$m_{S_{\mathrm{NHx}}\,g_{\mathrm{hAn}}} \coloneqq -\iota_{\mathrm{NXb}} \tag{56}$$

$$m_{S_{\mathrm{NHx}}\,g_{\mathrm{aO2}}} \coloneqq -\iota_{\mathrm{NXb}} - \frac{1}{\gamma_{\mathrm{a}}} \tag{57}$$

$$m_{X_{\mathrm{cbN}}\,d_{\mathrm{h}}} \coloneqq \iota_{\mathrm{NXb}} - \iota_{\mathrm{NXnb}}\zeta_{\mathrm{Xnb,l}} \tag{58}$$

$$m_{X_{\mathrm{cbN}}\,d_{\mathrm{a}}} \coloneqq \iota_{\mathrm{NXb}} - \iota_{\mathrm{NXnb}}\zeta_{\mathrm{Xnb,l}} \tag{59}$$

$$m_{S_{\mathrm{alk}}\,g_{\mathrm{hO2}}} \coloneqq -\iota_{\mathrm{NXb}}\iota_{\mathrm{cSNHx}} \tag{60}$$

$$m_{S_{\mathrm{alk}}\,g_{\mathrm{hAn}}} \coloneqq -\iota_{\mathrm{NXb}}\iota_{\mathrm{cSNHx}} + \frac{\iota_{\mathrm{cSNOx}}\left(\gamma_{\mathrm{h}} - 1\right)}{\gamma_{\mathrm{h}}\iota_{\mathrm{NO3,N2}}} \tag{61}$$

$$m_{S_{\mathrm{alk}}\,g_{\mathrm{aO2}}} \coloneqq \iota_{\mathrm{cSNHx}}\left(-\iota_{\mathrm{NXb}} - \frac{1}{\gamma_{\mathrm{a}}}\right) + \frac{\iota_{\mathrm{cSNOx}}}{\gamma_{\mathrm{a}}} \tag{62}$$

$$m_{S_{\mathrm{alk}}\,a_{\mathrm{N}}} \coloneqq \iota_{\mathrm{cSNHx}} \tag{63}$$

$$m_{S_{\mathrm{N2}}\,g_{\mathrm{hAn}}} \coloneqq \frac{1 - \gamma_{\mathrm{h}}}{\gamma_{\mathrm{h}}\iota_{\mathrm{NO3,N2}}} \tag{64}$$

$$\tag{65}$$

$$\boldsymbol{r} = \begin{bmatrix} g_{\mathrm{hO2}}(S_{\mathrm{NHx}}, S_{\mathrm{O2}}, S_{\mathrm{b}}, X_{\mathrm{h}}) \\ g_{\mathrm{hAn}}(S_{\mathrm{NHx}}, S_{\mathrm{NOx}}, S_{\mathrm{O2}}, S_{\mathrm{b}}, X_{\mathrm{h}}) \\ g_{\mathrm{aO2}}(S_{\mathrm{NHx}}, S_{\mathrm{O2}}, X_{\mathrm{a}}) \\ d_{\mathrm{h}}(X_{\mathrm{h}}) \\ d_{\mathrm{a}}(X_{\mathrm{a}}) \\ a_{\mathrm{N}}(S_{\mathrm{bN}}, X_{\mathrm{h}}) \\ h_{\mathrm{o}}(S_{\mathrm{NOx}}, S_{\mathrm{O2}}, X_{\mathrm{cb}}, X_{\mathrm{h}}) \\ h_{\mathrm{oN}}(S_{\mathrm{NOx}}, S_{\mathrm{O2}}, X_{\mathrm{cbN}}, X_{\mathrm{cb}}, X_{\mathrm{h}}) \end{bmatrix} \tag{66}$$

$$g_{\mathrm{hO2}}(S_{\mathrm{NHx}}, S_{\mathrm{O2}}, S_{\mathrm{b}}, X_{\mathrm{h}}) \coloneqq S_{\mathrm{NHx}} S_{\mathrm{b}} X_{\mathrm{h}} \mu_{\mathrm{max,h}} \frac{S_{\mathrm{O2}}}{\left(S_{\mathrm{NHx}} + \kappa_{\mathrm{NHx,h}}\right)\left(S_{\mathrm{O2}} + \kappa_{\mathrm{O2,h}}\right)\left(S_{\mathrm{b}} + \kappa_{\mathrm{b}}\right)} \tag{67}$$

$$g_{\mathrm{hAn}}(S_{\mathrm{NHx}}, S_{\mathrm{NOx}}, S_{\mathrm{O2}}, S_{\mathrm{b}}, X_{\mathrm{h}}) \coloneqq S_{\mathrm{NHx}} S_{\mathrm{b}} X_{\mathrm{h}} \mu_{\mathrm{max,h}} \frac{S_{\mathrm{NOx}} \eta_{\mathrm{an,h}} \kappa_{\mathrm{O2,h}}}{\left(S_{\mathrm{NHx}} + \kappa_{\mathrm{NHx,h}}\right)\left(S_{\mathrm{O2}} + \kappa_{\mathrm{O2,h}}\right)\left(S_{\mathrm{b}} + \kappa_{\mathrm{b}}\right)\left(S_{\mathrm{NOx}} + \kappa_{\mathrm{NOx,h}}\right)} \tag{68}$$

$$g_{\mathrm{aO2}}(S_{\mathrm{NHx}}, S_{\mathrm{O2}}, X_{\mathrm{a}}) \coloneqq \frac{S_{\mathrm{NHx}} S_{\mathrm{O2}} X_{\mathrm{a}} \mu_{\mathrm{max,a}}}{\left(S_{\mathrm{NHx}} + \kappa_{\mathrm{NHx,a}}\right)\left(S_{\mathrm{O2}} + \kappa_{\mathrm{O2,a}}\right)} \tag{69}$$

$$d_{\mathrm{h}}(X_{\mathrm{h}}) \coloneqq X_{\mathrm{h}} \beta_{\mathrm{h}} \tag{70}$$

$$d_{\mathrm{a}}(X_{\mathrm{a}}) \coloneqq X_{\mathrm{a}} \beta_{\mathrm{a}} \tag{71}$$

$$a_{\mathrm{N}}(S_{\mathrm{bN}}, X_{\mathrm{h}}) \coloneqq S_{\mathrm{bN}} X_{\mathrm{h}} \lambda_{\mathrm{am}} \tag{72}$$

$$h_{\mathrm{o}}(S_{\mathrm{NOx}}, S_{\mathrm{O2}}, X_{\mathrm{cb}}, X_{\mathrm{h}}) \coloneqq X_{\mathrm{cb}} \lambda_{\mathrm{hyd,b}} \frac{X_{\mathrm{h}}}{X_{\mathrm{cb}} + X_{\mathrm{h}} \kappa_{\mathrm{Xhyd}}} \left(\frac{S_{\mathrm{NOx}} \eta_{\mathrm{hyd,an}} \kappa_{\mathrm{O2,h}}}{\left(S_{\mathrm{NOx}} + \kappa_{\mathrm{NOx,h}}\right)\left(S_{\mathrm{O2}} + \kappa_{\mathrm{O2,h}}\right)} + \frac{S_{\mathrm{O2}}}{S_{\mathrm{O2}} + \kappa_{\mathrm{O2,h}}}\right) \tag{73}$$

$$h_{\mathrm{oN}}(S_{\mathrm{NOx}}, S_{\mathrm{O2}}, X_{\mathrm{cbN}}, X_{\mathrm{cb}}, X_{\mathrm{h}}) \coloneqq X_{\mathrm{cbN}} \lambda_{\mathrm{hyd,b}} \frac{X_{\mathrm{h}}}{X_{\mathrm{cb}} + X_{\mathrm{h}} \kappa_{\mathrm{Xhyd}}} \left(\frac{S_{\mathrm{NOx}} \eta_{\mathrm{hyd,an}} \kappa_{\mathrm{O2,h}}}{\left(S_{\mathrm{NOx}} + \kappa_{\mathrm{NOx,h}}\right)\left(S_{\mathrm{O2}} + \kappa_{\mathrm{O2,h}}\right)} + \frac{S_{\mathrm{O2}}}{S_{\mathrm{O2}} + \kappa_{\mathrm{O2,h}}}\right) \tag{74}$$

$$\tag{75}$$

$$\dot{S}_{\mathrm{b}} \coloneqq g_{\mathrm{hAn}} m_{S_{\mathrm{b}}\, g_{\mathrm{hAn}}} + g_{\mathrm{hO2}} m_{S_{\mathrm{b}}\, g_{\mathrm{hO2}}} + h_{\mathrm{o}} \tag{76}$$

$$\dot{X}_{\mathrm{cb}} \coloneqq d_{\mathrm{a}} m_{X_{\mathrm{cb}}\, d_{\mathrm{a}}} + d_{\mathrm{h}} m_{X_{\mathrm{cb}}\, d_{\mathrm{h}}} - h_{\mathrm{o}} \tag{77}$$

$$\dot{X}_{\mathrm{h}} \coloneqq -d_{\mathrm{h}} + g_{\mathrm{hAn}} + g_{\mathrm{hO2}} \tag{78}$$

$$\dot{X}_{\mathrm{a}} \coloneqq -d_{\mathrm{a}} + g_{\mathrm{aO2}} \tag{79}$$

$$\dot{S}_{\mathrm{O2}} \coloneqq g_{\mathrm{aO2}} m_{S_{\mathrm{O2}}\, g_{\mathrm{aO2}}} + g_{\mathrm{hO2}} m_{S_{\mathrm{O2}}\, g_{\mathrm{hO2}}} \tag{80}$$

$$\dot{S}_{\mathrm{NOx}} \coloneqq g_{\mathrm{aO2}} m_{S_{\mathrm{NOx}}\, g_{\mathrm{aO2}}} + g_{\mathrm{hAn}} m_{S_{\mathrm{NOx}}\, g_{\mathrm{hAn}}} \tag{81}$$

$$\dot{S}_{\mathrm{NHx}} \coloneqq a_{\mathrm{N}} + g_{\mathrm{aO2}} m_{S_{\mathrm{NHx}}\, g_{\mathrm{aO2}}} + g_{\mathrm{hAn}} m_{S_{\mathrm{NHx}}\, g_{\mathrm{hAn}}} + g_{\mathrm{hO2}} m_{S_{\mathrm{NHx}}\, g_{\mathrm{hO2}}} \tag{82}$$

$$\dot{S}_{\mathrm{bN}} \coloneqq -a_{\mathrm{N}} + h_{\mathrm{oN}} \tag{83}$$

$$\dot{X}_{\mathrm{cbN}} \coloneqq d_{\mathrm{a}} m_{X_{\mathrm{cbN}}\, d_{\mathrm{a}}} + d_{\mathrm{h}} m_{X_{\mathrm{cbN}}\, d_{\mathrm{h}}} - h_{\mathrm{oN}} \tag{84}$$

$$\tag{85}$$

$$\dot{X}_{\mathrm{nb,e}} \coloneqq d_{\mathrm{a}} m_{X_{\mathrm{nb,e}}\, d_{\mathrm{a}}} + d_{\mathrm{h}} m_{X_{\mathrm{nb,e}}\, d_{\mathrm{h}}} \tag{86}$$

$$\dot{S}_{\mathrm{alk}} \coloneqq a_{\mathrm{N}} m_{S_{\mathrm{alk}}\, a_{\mathrm{N}}} + g_{\mathrm{aO2}} m_{S_{\mathrm{alk}}\, g_{\mathrm{aO2}}} + g_{\mathrm{hAn}} m_{S_{\mathrm{alk}}\, g_{\mathrm{hAn}}} + g_{\mathrm{hO2}} m_{S_{\mathrm{alk}}\, g_{\mathrm{hO2}}} \tag{87}$$

$$\dot{S}_{\mathrm{N2}} \coloneqq g_{\mathrm{hAn}} m_{S_{\mathrm{N2}}\, g_{\mathrm{hAn}}} \tag{88}$$

$$\tag{89}$$

$$\dot{S}_{\mathrm{nb}} \coloneqq 0 \tag{90}$$

$$\dot{X}_{\mathrm{nb,in}} \coloneqq 0 \tag{91}$$

$$\tag{92}$$

This work	Other name	Value	Units	Description
M_N	M_N	14.0	$\mathrm{g\,mol^{-1}}$	atomic molar mass of nitrogen
$\mathrm{COD_C}$	COD_C	32.0	$\mathrm{g\,mol^{-1}}$	Theoretical COD of molar carbon
$\mathrm{COD_{Fe}}$	COD_Fe	24.0	$\mathrm{g\,mol^{-1}}$	Theoretical COD of molar iron
$\mathrm{COD_H}$	COD_H	8.0	$\mathrm{g\,mol^{-1}}$	Theoretical COD of molar hydrogen
$\mathrm{COD_N}$	COD_N	-24.0	$\mathrm{g\,mol^{-1}}$	Theoretical COD of molar nitrogen
$\mathrm{COD_O}$	COD_O	-16.0	$\mathrm{g\,mol^{-1}}$	Theoretical COD of molar oxygen
$\mathrm{COD_P}$	COD_P	40.0	$\mathrm{g\,mol^{-1}}$	Theoretical COD of molar phosphorus
$\mathrm{COD_S}$	COD_S	48.0	$\mathrm{g\,mol^{-1}}$	Theoretical COD of molar sulphur
$\mathrm{COD_+}$	COD_pos	-8.0	$\mathrm{g\,mol^{-1}}$	Theoretical COD of positive charge
$\mathrm{COD_-}$	COD_neg	8.0	$\mathrm{g\,mol^{-1}}$	Theoretical COD of negative charge
β_a	b_ANO	0.15	$\mathrm{d^{-1}}$	Decay rate for XANO (b_A)
β_h	b_OHO	0.62	$\mathrm{d^{-1}}$	Decay rate for XOHO (b_H)
$\eta_\mathrm{an,h}$	n_mOHOAx	0.8	$-$	Reduction factor for anoxic growth of XOHO (η_g)
$\eta_\mathrm{hyd,an}$	n_qhydAx	0.4	$-$	Correction factor for hydrolysis under anoxic conditions (η_h)
γ_a	Y_ANO	0.24	$\mathrm{g\,g^{-1}}$	Yield of XANO growth per SNO3 (Y_A)
γ_h	Y_OHO	0.67	$\mathrm{g\,g^{-1}}$	Yield for XOHO growth (Y_H)
$\iota_\mathrm{COD,N2}$	i_CODN2	$\mathrm{COD_N}/M_\mathrm{N}$	$\mathrm{g\,g^{-1}}$	Conversion factor for N2 in COD (i_CODN2)
$\iota_\mathrm{COD,NO3}$	i_CODNO3	$\left(\mathrm{COD_N} + 3\mathrm{COD_O} + \mathrm{COD_-}\right)/M_\mathrm{N}$	$\mathrm{g\,g^{-1}}$	Conversion factor for NO3 in COD (i_CODNO3)
$\iota_\mathrm{NO3,N2}$	i_NO3N2	$\left(-3\mathrm{COD_O} - \mathrm{COD_-}\right)/M_\mathrm{N}$	$\mathrm{g\,g^{-1}}$	Conversion factor for NO3 reduction to N2 (i_NO3N2)
ι_NXb	i_NXBio	0.086	$\mathrm{g\,g^{-1}}$	N content of biomass, meaning XOHO, XPAO, and XANO (i_XB)
ι_NXnb	i_NXUE	0.06	$\mathrm{g\,g^{-1}}$	N content of products from biomass (i_XE)
ι_cSNHx	$i_\mathrm{ChargeSNHx}$	$1/M_\mathrm{N}$	$\mathrm{mol\,g^{-1}}$	Conversion factor for NHx in charge ($i_\mathrm{ChargeSNHx}$)
ι_cSNOx	$i_\mathrm{ChargeSNOx}$	$-1/M_\mathrm{N}$	$\mathrm{mol\,g^{-1}}$	Conversion factor for NO3 in charge ($i_\mathrm{ChargeSNOx}$)
κ_b	K_SBOHO	20.0	$\mathrm{g\,m^{-3}}$	Half-saturation coefficient for SB (K_S)
$\kappa_\mathrm{NHx,a}$	K_NHxANO	1.0	$\mathrm{g\,m^{-3}}$	Half-saturation coefficient for SNHx for XANO (K_NH)
$\kappa_\mathrm{NHx,h}$	K_NHxOHO	0.05	$\mathrm{g\,m^{-3}}$	Half-saturation coefficient for NH4 (not in classic ASM1)
$\kappa_\mathrm{NOx,h}$	K_NOxOHO	0.5	$\mathrm{g\,m^{-3}}$	Half-saturation coefficient for SNOx XOHO (K_NO)
$\kappa_\mathrm{O2,a}$	K_O2ANO	0.4	$\mathrm{g\,m^{-3}}$	Half-saturation coefficient for SO2 for XANO (K_OA)
$\kappa_\mathrm{O2,h}$	K_O2OHO	0.2	$\mathrm{g\,m^{-3}}$	Half-saturation coefficient for SO2 XOHO (K_OH)
κ_Xhyd	K_XCBhyd	0.03	$\mathrm{g\,g^{-1}}$	Saturation coefficient for XB/XOHO (K_X)
λ_am	q_am	0.08	$\mathrm{m^3\,d^{-1}\,g^{-1}}$	Rate constant for ammonification (k_a)
$\lambda_\mathrm{hyd,b}$	q_XCBSBhyd	3.0	$\mathrm{g\,g^{-1}}$	Maximum specific hydrolysis rate of particulate and soluble biodegradable organics (k_h)
$\mu_\mathrm{max,h}$	m_OHOMax	6.0	$\mathrm{d^{-1}}$	Maximum growth rate of XOHO (μ_H)
$\mu_\mathrm{max,a}$	m_ANOMax	0.8	$\mathrm{d^{-1}}$	Maximum growth rate of XANO (μ_A)
$\zeta_\mathrm{Xnb,l}$	f_XUBiolys	0.08	$\mathrm{g\,g^{-1}}$	Fraction of XU generated in biomass decay (f_P)

Table 4: Parameters

State variable	min	reference	max	reference
S_{b}	0.9	reactor 5 [52]	69	[52]
S_{O2}	2	[16]	2.2	[16]
X_{cb}	49	reactor 5 [52]	82	reactor 1 [52]
S_{NHx}	1.7	reactor 5 [52]	8	reactor 1 [52]
S_{NOx}	6	reactor 1 [52]	10	reactor 5 [52]
X_{cbN}	0.01	reactor 1 [52]	3.5	reactor 5 [52]
S_{bN}	0.7	reactor 5 [52]	2	reactor 1 [52]
X_{h}	2304	reactor 5 [52]	2816	reactor 1 [52]
X_{a}	135	reactor 5 [52]	165	reactor 1 [52]

Table 5: Scenario 1 for range of concentrations in the reactor that the wastewater treatment process is designed for. Most values are taken from the BSM1 [52]. The dissolved oxygen S_{O2} concentration is an exception as the model is not for a sequencing batch reactor and we used the values that we observed in an sequencing batch reactor. With this selection method X_{h} and X_{a} have the same value which is not suitable for our approach. Hence we took for the maximum +10% and for the minimum -10% from the value in the BSM1 which are 2560 respectively 150.

State variable	min	reference	max	reference
S_{b}	0	-	2560	[53]
S_{O2}	0	-	8	saturation concentration
X_{cb}	0.2	effluent [52]	91	mean of reactor 1 and underflow [52]
S_{NHx}	0	-	400	assumption based on [54]
S_{NOx}	0	-	400	assumption based on [54]
X_{cbN}	0.01	effluent [52]	6.5	mean of reactor 1 and underflow [52]
S_{bN}	0.7	reference	320	[55]
X_{h}	10	effluent [52]	3780	mean of reactor 1 and underflow [52]
X_{a}	0.6	effluent [52]	225	mean of reactor 1 and underflow [52]

Table 6: Scenario 2 for range of concentrations in the reactor which could happen in for example on-site wastewater treatment facilities. The assumption based on Dockhorn et al. [54] is made that all nitrogen produces per day is present as NHx respectively NOx and that 60 liters of water are consumed per day.

State variable	min	reference	max	reference
S_{b}	0	-	8200	observed maximum[56]
S_{O2}	0	-	8	saturation concentration
X_{cb}	0	-	100	underflow [52]
S_{NHx}	0	-	300000	saturation concentration
S_{NOx}	0	-	9000	fertiliser production [57]
X_{cbN}	0	-	7	underflow [52]
S_{bN}	0	-	320	[55]
X_{h}	0	-	5000	underflow [52]
X_{a}	0	-	300	underflow [52]

Table 7: Scenario 3 for range of concentrations in the reactor which are physically possible, though many probably unlikely to happen.

C Causal diagram

Confounding situations are when one sees an association (correlation) but there is no causal relationship. A mediator M (X -> M -> F) might be present or the situation is spurious (X <- F -> Y), which means that there is no causal relation that leads to the correlation between the two elements X and Y. Another situation in causal diagrams is a collider (X -> F <- Y), which is also called a V-structure or immorality and is the structure that we observed between the different states of the ASM1 and the ramp feature. The V-structure means that not only the variable of interest X leads to feature F ($S_{\mathrm{NHx}} <$ threshold), but also several other state variables such as Y.

C.1 Ammonium depletion soft-sensor based on the dissolved oxygen ramp feature

In a previous study [16], the soft sensor for a maintained dissolved oxygen sensor reached a 93% accuracy with the ramp feature for a balanced dataset where half of the data had an ammonium concentration below or equal to a threshold T and half the data was above. The arbitrary threshold was chosen as double the amount of the detection limit of the ammonium measurements in the laboratory (i.e. $1\,\mathrm{g\,m^{-3}}$). For the unmaintained sensor, it was 80%. A high prediction accuracy could be achieved despite our study exposing alternative causes for the ramp.

In the previous study, we chose the most challenging real-world cases to which we were granted access. Additionally, we used synthetic, modelled data to make the feature fail to validate the feature and still obtained a wide range with high prediction accuracy [6].

Nevertheless, despite the rigour that we used, the results of the DSA in this article clearly advise caution when barely deciding on fit in data-matching if a prediction is good enough or not. Especially in the face of climate change or on-site applications where conditions outside the training data set are likely to occur. This supports the statement by Zhong et al. who show the power of data-driven tools, but also caution that they should not be overly trusted either. DSA hence should indeed be applied much more frequently to decide if a feature is really robust or needs to be further refined or combined with other features, as the ramp feature will have to be.